ISPRS Journal of Photogrammetry and Remote Sensing 137 (2018) 29–46

Contents lists available at ScienceDirect

ISPRS Journal of Photogrammetry and Remote Sensing

journal homepage: www.elsevier.com/locate/isprsjprs

Harmonic regression of Landsat time series for modeling attributes from national forest inventory data

Barry T. Wilson [a,*], Joseph F. Knight [b], Ronald E. McRoberts [a]

[a] Northern Research Station, USDA Forest Service, 1992 Folwell Avenue, St. Paul, MN 55108 USA
[b] Department of Forest Resources, University of Minnesota, 1530 Cleveland Avenue N., St. Paul, MN 55108 USA

A R T I C L E I N F O

Article history:
Received 7 September 2017
Received in revised form 2 January 2018
Accepted 7 January 2018

Keywords:
Landsat time series
Image compositing
Harmonic regression
National forest inventory
Regression models
Classification models

A B S T R A C T

Imagery from the Landsat Program has been used frequently as a source of auxiliary data for modeling land cover, as well as a variety of attributes associated with tree cover. With ready access to all scenes in the archive since 2008 due to the USGS Landsat Data Policy, new approaches to deriving such auxiliary data from dense Landsat time series are required. Several methods have previously been developed for use with finer temporal resolution imagery (e.g. AVHRR and MODIS), including image compositing and harmonic regression using Fourier series. The manuscript presents a study, using Minnesota, USA during the years 2009–2013 as the study area and timeframe. The study examined the relative predictive power of land cover models, in particular those related to tree cover, using predictor variables based solely on composite imagery versus those using estimated harmonic regression coefficients. The study used two common non-parametric modeling approaches (i.e. *k*-nearest neighbors and random forests) for fitting classification and regression models of multiple attributes measured on USFS Forest Inventory and Analysis plots using all available Landsat imagery for the study area and timeframe. The estimated Fourier coefficients developed by harmonic regression of tasseled cap transformation time series data were shown to be correlated with land cover, including tree cover. Regression models using estimated Fourier coefficients as predictor variables showed a two- to threefold increase in explained variance for a small set of continuous response variables, relative to comparable models using monthly image composites. Similarly, the overall accuracies of classification models using the estimated Fourier coefficients were approximately 10–20 percentage points higher than the models using the image composites, with corresponding individual class accuracies between six and 45 percentage points higher.

1. Introduction

The use of remotely sensed data for inventory and mapping of agricultural and natural resources has a long history. Such data have typically been collected on airborne or spaceborne platforms by either passive sensors that use solar radiation as a source of electromagnetic energy, or active sensors that provide their own radiation source. Both passive and active sensors have demonstrated utility as sources of predictor variables that can be used to model a variety of natural resource phenomena.

In the context of using these data in combination with national forest inventory (NFI) data for the purposes of monitoring forest resources over long periods of time and large geographic areas, the Landsat platform has garnered particular interest, as noted by the review of McRoberts et al. (2010a). This is due to several factors, which will be discussed in greater detail below. First, the Landsat Program provides the longest-running continuous collection of Earth imagery of any satellite program, with sensors designed to maintain consistency in resolution (i.e. spatial, spectral, radiometric, and temporal) across missions. Second, the multispectral characteristics of the Landsat sensors enable the derivation of metrics with biophysical meaning. Third, the spatial resolution of the latter generation of sensors provides a better match to the size of the typical NFI plot than that of satellite sensors with coarser spatial resolution. Finally, with the adoption of the open access data policy for the Landsat Program in 2008, the entire archive of Landsat imagery is freely available for use.

1.1. Landsat as a source of auxiliary data

1.1.1. Length of the Landsat record

From the Multispectral Scanner (MSS) sensor used onboard the first five Landsat satellites to the Thematic Mapper (TM) sensor of

* Corresponding author.
E-mail address: barrywilson@fs.fed.us (B.T. Wilson).

https://doi.org/10.1016/j.isprsjprs.2018.01.006
0924-2716/Published by Elsevier B.V. on behalf of International Society for Photogrammetry and Remote Sensing, Inc. (ISPRS).

Landsat-4 and Landsat-5, the Landsat program has striven for consistency in the data record while simultaneously incorporating improved technological capabilities in terms of spatial and spectral resolution. This consistency extends to the sensors used onboard the Landsat satellites in orbit today, as well as those planned for future missions.

One of the two Landsat sensors currently in operation is the Landsat-7 Enhanced Thematic Mapper Plus (ETM+). In May of 2003, the Landsat-7 scan line corrector (SLC), a small rotating mirror that compensates for the forward motion of the spacecraft, failed. This resulted in the loss of data in wedge-shaped areas on either side of the image, with more missing data further away from nadir. These SLC-off gaps amount to a loss of approximately 22% of the data for any given scene (Ju and Roy, 2008). These gaps have limited the utility of ETM+ imagery, although there have been several approaches proposed to dealing with them, including compositing of several images (Roy et al., 2010), interpolation using SLC-on imagery (Maxwell et al., 2007; Chen et al., 2011), data fusion with MODIS imagery (Roy et al., 2008), and geostatistical methods (Zhang et al., 2007; Pringle et al., 2009).

1.1.2. Development of Landsat spectral indices

Multiple spectral indices have been developed to establish the relationship between the spectral and radiometric response measured by remote sensors and the presence of various land covers, especially vegetation. Bannari et al. (1995) reviewed over forty vegetation indices that have been developed for sensors ranging from ground-based to spaceborne systems. Most such indices are based on the fact that vegetation has wavelength-dependent absorption, transmission, and reflection properties, in particular the differential response in the red and near-infrared (NIR) wavelengths, and have been shown to provide a better indication of the amount of vegetative land cover than any single band alone (Curran, 1980).

Kauth and Thomas (1976) developed a linear transformation of all four of the original MSS bands, named the tasseled cap transformation (TCT), to produce indices related to not only growing vegetation ('green stuff'), but also soils ('brightness'), senescent vegetation ('yellow stuff'), and shadows ('non-such') to better differentiate various crops, as well as phases of crop development over time. Crist and Cicone (1984a, 1984b) extended TCT for use with the six reflective TM bands, simultaneously dropping some features ('yellow stuff' and 'non-such') while defining new ones (e.g. 'wetness'). Huang et al. (2002) and Baig et al. (2014) developed comparable transformations for ETM+ and the Operational Land Imager (OLI) respectively.

Numerous studies have shown TCT components derived from Landsat imagery to be useful for mapping forest characteristics. These studies, using the components of brightness, greenness, and/or wetness, demonstrate their utility across a range of forest mapping applications, including land cover (Byrne et al., 1980; Yuan et al., 2005), forest types (Dymond et al., 2002), succession (Helmer et al., 2000), stand-replacing disturbance (Cohen et al., 1998; Jin and Sader, 2005; Healey et al., 2005), pest damage (Skakun et al., 2003), growing stock volume (Zheng et al., 2014), canopy cover and biomass (Karlson et al., 2015), and recovery from disturbance (Pickell et al., 2016).

1.1.3. Size and configuration of the NFI plot footprint

The current annual NFI conducted by United States Forest Service Forest Inventory and Analysis (FIA) program exhibits many of the characteristics observed for NFI globally that are pertinent to its use with Landsat imagery. A comprehensive description of the FIA program is provided in Bechtold and Patterson (2005). FIA inventory plots are established according to a well-defined sample design, with a sampling frame that is used to generate a spatially-balanced sample of plots. Each plot is a cluster of sub-plots. Cluster plots are often used for NFI because the determination of the relative locations of the sub-plots is typically more accurate, their layout is generally faster due to the smaller distances measured and traveled (possibly over rugged terrain), and they capture more variability in the population than one larger plot (Kangas and Maltamo, 2006).

Since the nationwide start of the annual NFI program in the US in 1998, FIA plots comprise four circular sub-plots, each with a radius of 7.3152 m. Circular plots are often used in forest inventory because they are easy to establish for small radii and are prone to less error in plot area, for the same reasons given previously for using cluster plots (Kangas and Maltamo, 2006). Circular plots also minimize edge effects, since they have the smallest possible perimeter for a given area by the isoperimetric inequality. The sub-plots are arranged with the center of one sub-plot defining the center of the cluster plot. The centers of each of the other three sub-plots are equally spaced about plot center, oriented so one sub-plot is due north of plot center, and each is 36.576 m distant from plot center.

Although other NFI programs have different sample designs, sampling frames, and plot configurations, the information presented for the FIA program remains instructive for comparisons to Landsat and other satellite imagery. Each FIA sub-plot constitutes an area of about 168 m^2, approximately 19% the area of a TM, ETM+, or OLI pixel for the reflective bands, but only about 0.27% the area of a 250-m MODIS pixel. The smallest circle that circumscribes all four sub-plots has an area of about 6052 m^2, or just under seven 30-m pixels. The four sub-plots cover approximately 11% of this area, and about 1% of the area of a MODIS pixel.

1.1.4. Open data access policy for the Landsat archive

Ease of access to data from the Landsat Program has been variable over time. During the commercial operations period, there were high financial costs and restrictive copyright rules in place that limited sharing of access to imagery. With the assumption of mission operations by the United States Geological Survey (USGS), purchased imagery could be shared more freely. Wulder et al. (2012) suggest that the USGS Landsat Data Policy that took effect in 2008 has allowed the scientific community to finally realize the full value of the Landsat Program, as indicated by the dramatic rise in the use of its data globally. This data policy provides unrestricted access to the entire USGS National Satellite Land Remote Sensing Data Archive (NSLRSDA), with selected products made available for retrieval over the Internet at no financial cost to users (Woodcock et al., 2008).

1.2. Approaches to analyzing dense time series of satellite imagery

Free and open access to the Landsat Archive (i.e. NSLRSDA) permits new approaches to image analysis that were not previously available to users of Landsat imagery. With the high costs of Landsat scenes under earlier data policies, users typically selected only those scenes of interest that were predominantly free of clouds, exhibiting a 'scene-centric' focus. Under the new data policy, as well as due to continuing advancements in data storage and computing power, users have begun developing methods that utilize all scenes over a period of interest to improve the information collected for pixels of interest, shifting to a 'pixel-centric' focus.

There are several approaches to processing and analyzing dense time series of satellite imagery. Most were developed for use with other satellite platforms, particularly those having finer temporal resolution than Landsat. One of the first was published by Goward et al. (1985) for analyzing daily observations of NDVI across North America using the Advanced Very High Resolution Radiometer (AVHRR) onboard the NOAA-7 satellite. The daily data were grouped into three-week bins, and the maximum value for each pixel from each bin was used as the bin's composite value, thereby reducing the effects of cloud contamination. These maximum value composites (MVC) were computed for a 30-week growing season and used to estimate the variability and area under the seasonal Normalized Difference Vegetation Index (NDVI) profile for each pixel. Both metrics were shown to be correlated with seasonal patterns in natural and cultivated vegetation, as well as net primary productivity.

Reed et al. (1994) took a similar approach for a study using AVHRR data to map land cover types for the conterminous US. Four growing seasons of biweekly MVC NDVI were used to develop a set of 12 seasonal NDVI metrics. These included not only NDVI range and area under the curve, as used in the study by Goward et al. (1985), but also time and value at onset and end of greenness and derived rates of green-up and senescence along with a few other metrics. The authors noted some limitations of using biweekly MVC images, such as the compositing period being too long to determine some phenological events and residual cloud contamination. Nevertheless, the results indicated strong agreement with expected characteristics for various land cover types, including assorted agricultural crops, grasslands, shrublands, and forests. DeFries et al. (1995) reported similar results for a study using AVHRR MVC data for global land cover mapping.

Sellers et al. (1994, 1996) were among the first to use a mathematical model to describe time series of AVHRR NDVI data in an effort to correct for residual cloud contamination in MVC images. The complete methodology they proposed included a series of steps, with the first being adjustment of the MVC values by means of a Fourier series. A Fourier series can be used to approximate a periodic function, such as the seasonality of NDVI, with a closer approximation given by using more harmonics in the series. This application of Fourier series is also known as harmonic analysis or harmonic regression. Other harmonic regression methods have also been developed to produce cloud-free AVHRR images (Roerink et al., 2000).

Moody and Johnson (2001) conducted a study to map land cover for a small area in southern California, USA, using AVHRR NDVI monthly MVC images. The coefficients for a Fourier series with two harmonics were estimated for each pixel in the study area. These coefficients were used as feature variables with an unsupervised classification scheme to produce a map of six basic vegetation formations. Comparison with field-based validation data yielded an overall accuracy of 68%. The authors found that the estimated mean NDVI provided discrimination along a continuum from grassland to closed canopy forest, amplitude separated evergreen from deciduous vegetation, and phase distinguished grasslands from shrublands/woodlands/forests and irrigated croplands.

Alternative methods for describing AVHRR time series data have been proposed, using models such as the asymmetric Gaussian (Jönsson and Eklundh, 2002) and the Savitzky-Golay filter (Chen et al., 2004). Hermance (2007) and Bradley et al. (2007) suggested enhancements to the original harmonic regression methods intended to address the issue of higher-order harmonics generating spurious oscillations identified in the two aforementioned studies. Others studies have employed similar approaches with MODIS time series data, using harmonic regression (Potgieter et al., 2007; Geerken, 2009; Wilson et al., 2012), piecewise logistic models (Zhang et al., 2003), the wavelet transform (Sakamoto et al., 2005), cubic splines (Scharlemann et al., 2008), and the autoregressive integrated moving average (Bayr et al., 2016). Hird and McDermid (2009) conducted a thorough comparison of several of these techniques for reducing noise in NVDI time series of MODIS imagery and concluded that the double logistic and asymmetric Gaussian approaches were generally superior to the others in the study. However, they also cautioned that their conclusions were conditional on the nature of the noise in the imagery.

1.3. Using Landsat time series data for vegetation modeling and mapping

Many of the studies reviewed in the previous section primarily focused on methods to remove noise from satellite image time series in coarse spatial resolution satellite imagery. There are comparable studies in the literature that use Landsat imagery. For example, Brooks et al. (2012) demonstrated the effectiveness of using harmonic regression to model NDVI time series derived from TM and ETM+ imagery. Other studies previously reviewed focused instead on the use of these seasonal characteristics to produce models and maps of vegetation. A few such applications using AVHRR and MODIS imagery include mapping net primary productivity (Goward et al., 1985), land cover (Reed et al., 1994; DeFries et al., 1995; Moody and Johnson, 2001), and tree species relative abundance (Wilson et al., 2012).

In terms of mapping vegetation with finer spatial resolution imagery, Badhwar et al. (1982) developed one of the earliest such applications, using temporal profiles of TCT greenness derived from MSS imagery. A nonlinear model was used to fit TCT greenness time series via an iterative Marquardt technique. The two estimated model parameters for each pixel were then used to classify 40 small cropland test sites into 'corn', 'soybean', and 'other' crops. The authors found that the estimated model parameters were closely related to the target of interest, and suggested that the inclusion of other TCT metrics could improve the results.

After the implementation of the 2008 open data policy for the NSLRSDA, Zhu et al. (2012) demonstrated that harmonic regression of dense TM and ETM+ time series could be used to map forest disturbance. After masking out clouds and cloud shadows, a Fourier series was fit on a per-pixel basis to the time series of surface reflectance for each reflective band in a 3600 km^2 study area on the border between Georgia and South Carolina, USA. A measure of forest disturbance was predicted by comparing predicted image values, based on the harmonic regression model parameters estimated for each pixel, with the observed image values. The accuracy assessment of the resultant maps of forest disturbance, based on manual interpretation of the Landsat imagery combined with finer resolution imagery, demonstrated user's and producer's accuracies of greater than 95% for classification into 'forest disturbance' and 'stable forest' classes.

Hansen et al. (2013) developed a method for mapping forest change at a global scale that leveraged not only the opening of the Landsat Archive and some of the analysis techniques reviewed here, but also the advent of cloud-based computing platforms. This massive study, spanning all global land except for the Arctic and Antarctic regions, used over 650,000 growing season ETM+ scenes collected between 2000 and 2012. The Landsat data were processed using Google Earth Engine (GEE), a platform for global scientific analysis and visualization of geospatial datasets (Gorelick et al., 2017). The raw ETM+ data were pre-processed by conversion to top-of-atmosphere (TOA) reflectance, screening for clouds, shadows, and water, and normalization using MODIS imagery. Three groups of seasonal metrics were derived from each band of the pre-processed data. These derived metrics were used as predictor variables in a model to predict forest cover, loss, and gain over the time period of the study.

1.4. Summary of the literature review

The preceding literature review covered multiple justifications for using Landsat time series imagery with NFI, and in particular FIA data for modeling and mapping land cover or use and especially characteristics of forest resources. These include the long history of the Landsat program and its temporal and geospatial overlap with the annual FIA program, the configuration of the FIA plot and sub-plots and their relative size compared to a Landsat pixel, and the institution of the 2008 open data policy for the Landsat Archive and concomitant development of cloud-based computing platforms like GEE that can readily access and process large volumes of data. It also touched upon the development of spectral indices for monitoring vegetation using satellite imagery as well as a variety of methods for analyzing time series of satellite imagery, from image compositing to the use of mathematical models for predicting seasonality in spectral reflectance associated with vegetative land cover. Finally, it provided examples of how these techniques were used to model vegetation, or changes in vegetation over time.

The literature review provided some examples of studies that have thoroughly examined individual elements of the problem at hand, such as the Hird and McDermid (2009) comparison of noise-reduction techniques in NDVI time series. However, there has not been one that explicitly examines the utility harmonic regression of dense time series of TCT metrics derived from TM and ETM+ data to extract auxiliary data for the modeling of forest attributes from NFI data. Therefore, a study is proposed here that will test the primary hypothesis that models using estimated harmonic regression coefficients will produce more accurate predictions than those based on composite images of dense Landsat time series alone. Furthermore, there is a secondary hypothesis associated with the proposed approach for modeling and mapping forest attributes using time series of Landsat imagery, namely that harmonic regression provides a means for overcoming missing data due to either weather-related phenomena like clouds and snow cover, or to instrument related gaps from the SLC failure.

2. Materials and methods

2.1. Study area and data

The study area and timeframe were selected to coincide with an area and timeframe covered by annual forest inventory data collection. The NFI conducted by FIA is based on the annual collection of data from a permanent plot sample of the population. The period over which all plots are measured ranges from either five or seven years in the eastern US to 10 years in the western US, meaning that 10–20% of the plots are measured each year. The sampling intensity of the FIA plot network is approximately one plot per 2400 ha. Some state partners of the FIA program contribute additional funds to increase the sampling intensity. The state of Minnesota is one such partner, and has augmented FIA funding to support an increase in sampling intensity to one plot per 1200 ha and to retain a measurement cycle of five years.

Because of the combination of a relatively large number of FIA plots due to its land area and a high sampling intensity, as well as the authors' familiarity with the state's forested ecosystems based on previous studies, Minnesota was chosen as the study area. In order to match the time period needed to collect a complete cycle of data for the FIA survey, all TM and ETM+ scenes for the timeframe of 2009–2013 were used. Furthermore, this five-year period provides a larger sample of sensor observations (across years) for each pixel from which to develop a harmonic regression model and increases the likelihood of filling any voids in the seasonal record due to clouds, snow, or SLC-off artifacts.

In the public FIA database (FIADB), an EVALID uniquely identifies a collection of plots used for producing estimates for a specific group of population attributes. All plots included in the FIA sample for the state of Minnesota during the study timeframe 2009–2013 for estimating condition area and tree volume were used in the analysis, corresponding to 'EVALID = 271303'. Out of a total of 17,500 plots in this collection, a subset of 17,343 was located inside the study area defined using the census boundary for the state of Minnesota stored in the Google cloud computing platform. For each of these plots, a set of 10 forest inventory response variables were extracted from FIADB for the central sub-plot in the cluster, in order to more closely match the spatial extent sampled by a single Landsat TM or ETM+ pixel. Categorical (2) and continuous (8) variables were chosen to examine the utility of the predictor variables under both classification and regression models.

The categorical variables used were the class assignment of the condition, corresponding to an area with similar land use and cover characteristics, at the center of the central sub-plot under two classification schemes. The first scheme assigned the condition to either the 'non-forest' or 'forest' class. The second scheme assigned the condition to one of five non-forest and three forest classes: 'water', 'cropland', 'grassland', 'settlement', 'wetland', 'coniferous forest', 'broadleaf forest', or 'non-stocked forest'. These schemes were chosen to be representative of a range of land cover and use classification levels.

The continuous variables used were the per hectare values of the number, basal area, foliage biomass, and total aboveground biomass of all live trees at least 2.54 cm diameter at breast height on the central sub-plot. The same set of attributes was also calculated for only live broadleaf trees. These variables were selected to be representative of a range of forest inventory attributes, based on counts (number), areas (basal area), and volumes (biomass), and by their nature would be expected to have varying correlations with the multispectral signal detected by the Landsat sensors. Furthermore, the variables associated with live broadleaf trees were chosen to evaluate the utility of dense time series of Landsat imagery for differentiation between deciduous and evergreen vegetation.

2.2. Image processing

Given the large volume of imagery required for the study, the GEE platform was used for processing the TM and ETM+ data. GEE provides ready access to registered users to data in the Landsat Archive, as well as a browser-based programming interface to process the imagery and store the results using Google's cloud computing infrastructure.

The number of remote sensing observations collected for a pixel depends on its location within the Worldwide Reference System (WRS) used to catalog Landsat data. There are four distinct zones of overlap in WRS-2, which is used to catalog both TM and ETM+ data, determined by the amount of overlap among adjacent scenes. There are overlap zones (1) with both sidelap and endlap, (2) with sidelap, (3) with endlap, and (4) with neither sidelap nor endlap. Endlap is the area of overlap between adjacent scenes along the path of the satellite. Sidelap is the area of overlap between adjacent scenes on neighboring paths. It should be noted that areas of endlap contain duplicate observations, since a single observation for a given pixel appears in adjacent scenes along the path of the satellite and were collected on the same day. Areas of sidelap do not contain duplicate observations, since the observations for a given pixel are collected on different days.

Landsat Level-1T (L1T) TOA reflectance data for the 6 reflective bands of TM and ETM+, along with the collection timestamp, were extracted from the Landsat Archive for the study area and timeframe. A total of 4425 images covering 25 WRS-2 Path/Row scene centers were used in the study, with 1575 from Landsat-5 and 2850 from Landsat-7. Although the temporal resolution for approximately the first three years of the study was eight days, it dropped to 16 days for the remainder due to the end of Landsat-5 operational image collection in November 2011. Therefore, a compositing period of about 52 days (i.e. 1/7 of a year) was chosen to ensure that there were at least three unique observations of each pixel for each compositing period in the study timeframe. This resulted in 35 composite images for the study timeframe.

The 52-day composite images were created by first masking out the observations most likely contaminated by clouds or snow, as well as any data flagged as missing during L1T processing, such as data located in SLC-off gaps. A built-in GEE cloud-scoring algorithm, based on the tendency of clouds to have higher reflectance values in blue, visible, and NIR bands but lower values in thermal infrared bands, was used to compute cloud metrics. The Normalized Difference Snow Index (NDSI) was used to compute snow metrics, and is based on the normalized difference of the green and first shortwave infrared (SWIR) bands (Hall et al., 1995). Only pixels with both a cloud score less than 75 and NDSI less than 0.5 were used to create the composite images.

Maximum value composites have often been used with NDVI data, because NDVI values have been shown to be lower in the presence of clouds and snow than they would be otherwise. Median value composites were used in this study, since the effect associated with the presence of clouds and snow could be either positive or negative depending on the spectral band. Furthermore, the median is a more accurate measure of central tendency than the mean when dealing with data that are highly skewed, as is the case for TOA values from any pixels having residual cloud or snow contamination not filtered out by the masking procedure. Each 52-day TOA composite image was generated by computing every pixel's median value for each band, including the image timestamp extracted from the scene metadata, from the set of observations passing through the cloud and snow filters.

The TCT coefficients developed by Huang et al. (2002) for ETM+ data were used to compute brightness, greenness, and wetness metrics for each composite image. Although composite images might include data from either TM or ETM+, the TCT coefficients developed by Crist and Cicone (1984a, 1984b) for TM data were not used. This choice was made for two reasons. First, it simplified the compositing procedure. Second, it was not readily apparent that the additional set of TCT coefficients would accentuate or mitigate any discrepancies between the data collected by TM and ETM+, since the two sensors have the same spatial and spectral characteristics in the reflective bands and the appropriate sensor metadata had already been used to compute TOA reflectance values.

2.3. Harmonic regression models

Ordinary least squares (OLS) regression was used to fit separate Fourier series to each composite time series of the three TCT metrics for each pixel in the study area. A form of the Fourier series based on the one presented in Sellers et al. (1996) was used in the analysis. Each time series of data was approximated as a trigonometric polynomial,

$$\widehat{Y}_t = a_0 + \sum_{j=1}^{m} a_j \cos(j2\pi t/n) + b_j \sin(j2\pi t/n),$$

where t is the composite timestamp value, n is the length of the cycle, and m is the order of the polynomial and equal to the number of harmonics in the approximation. Landsat image timestamps are stored as milliseconds since the start of the epoch (January 1, 1970) and were converted to fractional ephemeris days. A value of 365.2421891 ephemeris days per tropical year was used as the length of the annual cycle.

Regression models with one to four harmonics (i.e. 1st order to 4th order Fourier series) were tested to determine the model form that provided the best fit to the data without introducing the spurious oscillations noted by Hermance (2007) and Bradley et al. (2007). Geerken (2009) likewise suggested using between three and five harmonics for time series imagery, noting that between 81 and 99% of variance in a MODIS reference dataset was explained by a 3rd order Fourier series. These harmonics correspond to cycles of approximately 12, six, four, and three months respectively. The estimated coefficients from these Fourier series were stored as three-, five-, seven-, and nine-band images respectively, depending on the number of harmonics used in the regression model, resulting in nine, 15, 21, or 27 coefficients in total. The root mean squares of the residual errors (RMSE) for each order of Fourier series were also stored as three-band images. These RMSE images were used only for evaluation of the harmonic regression models, and not as auxiliary data for the modeling of forest attributes from NFI data.

2.4. Models of forest attributes

Because both classification and regression were required due to the nature of the response variables selected for the study, the non-parametric methods of random forests (RF) and k-nearest neighbors (kNN) were used to construct individual models relating the dense time series of Landsat imagery to the set of 10 forest inventory variables. Both methods have been used extensively in modeling and mapping applications that integrate satellite imagery and NFI data. McRoberts et al. (2010b) provide an excellent review of parametric and non-parametric modeling approaches that have been used for combining these data sources, including examples of both kNN and RF applications.

A brief description of the kNN (Fix and Hodges, 1951) and RF (Breiman, 2001) methods will be presented here, using similar terminology to that presented in McRoberts et al. (2010b). The set of population units for which both the predictor and response variables have been observed is designated the reference set. The set of population units for which predictions of response variables are desired is designated the target set. The space defined by the predictor variables is designated the feature space. A kNN prediction for a unit in the target set is made by calculating the mean (for continuous variables) or mode (for categorical variables) of the observed response variable for the k units in the reference set that are nearest to the unit in the target set in the feature space with respect to a distance metric. The kNN approach is usually optimized by the modeler, via the choice of k, the distance metric, the set of weights used to calculate the mean or mode, and the set of predictor variables used to construct the feature space (McRoberts, 2009a).

The RF method is an ensemble approach that requires the construction of a random set of decision trees (i.e. a forest of trees), each of which recursively partitions the reference set using threshold values along individual dimensions of the feature space onto leaves containing population units with similar observed response variables. The stochastic processes by which the trees are constructed include bootstrapping of reference units and random selection of predictor variables in the feature space. An RF prediction for a unit in the target set is made by first assigning the unit to a leaf in each tree in the forest according to the decision rules of the given tree. For each tree in the forest, the target unit is then assigned the mean or mode of the observed response variable for all reference units on the leaf to which it was assigned. Finally, the target unit is assigned the mean or mode of these predictions across all trees in the forest. Unlike kNN, RF typically does not require optimization by the modeler.

Two distinct sets of predictor variables derived from the dense time series of Landsat imagery were used to construct the feature space for the kNN and RF models. The first feature space was constructed from the seven mean monthly composites, approximately corresponding to the growing season in Minnesota of April to

October, of the 3 TCT metrics of brightness, greenness, and wetness. These mean monthly composites were derived by first creating the 60 monthly median value composites of TCT metrics covering the study timeframe, extracting the subset of 35 monthly growing season composites, then calculating the average TCT metric values by month across the five-year timeframe of the study. The second feature space was constructed from the estimated coefficients for each time series of 52-day composites of the 3 TCT metrics using 3rd order Fourier series, resulting in seven coefficients per series and matching the 21 dimensions of the composite feature space.

The *k*NN models were fitted using the 'rflann' package in R, which provides an interface to the Fast Library for Approximate Nearest Neighbors (Muja and Lowe, 2009). For each distinct feature space, the 'Neighbour' function was called with the default parameters of a kd-tree search with minimal checks on the precision of the result. This function was used to construct a list of the 200 nearest neighbors of each of the 17,343 plots in the study, treating these population units as both reference and target set, conditional on the given feature space. Because a reference unit will always be among its own nearest neighbors, a leave-one-out cross-validation approach was taken to optimize the choice of the value of *k*. Leave-one-out cross validation is the particular instance of the more familiar *K*-fold cross validation when *K* is equal to the number of observations. In the case of a *k*NN model, each observation in turn is withheld and used as the target unit, while the remaining observations are used as the reference set. The same effect can be achieved by including all observations in both the reference and target sets in a single *k*NN model, then excluding the first nearest neighbor when finding the set of *k*-nearest neighbors for each target unit.

One of the most appealing aspects of the kNN approach is that the set of *k*-nearest neighbors identified in the given feature space can be used to make multivariate predictions, under the assumption that predictor variables that are correlated with one response variable will also be correlated with the others. The current study also assumes that relationship and uses the same feature space for all *k*NN models. However, to allow for fairer comparison with RF model results, the optimal value of *k* was allowed to vary among *k*NN models to maximize the correlation between the predictor variables and each individual response variable. Excluding the reference unit itself, for regression models the coefficient of determination (R^2) was calculated for each model with *k* ranging from one to 199, with the predicted value for each unit being the unweighted mean of the observed continuous response variable for the *k* nearest neighbors. Similarly for classification models, excluding the reference unit itself, the overall accuracy (i.e. the percentage of the sample units that were correctly classified according to the plot data) was calculated for each model with *k* ranging from one to 199, with the predicted value for each unit being the mode of the observed categorical response variable for the *k* nearest neighbors. The value of *k* that maximized R^2 or the overall classification accuracy determined the optimal model given the feature space. No other optimization of the *k*NN models was attempted, because the purpose of the study was a comparison of the two feature spaces used for modeling, not a comparison of the two modeling approaches used. Individual class accuracies were also assessed using producer's accuracy (i.e. the percentage of sample units that were correctly classified for a given class in the plot data) and user's accuracy (i.e. the percentage of sample units that were correctly classified for a given class in the pixel data).

The RF models were fitted using the 'randomForest' package in R (Liaw and Wiener, 2002). For each combination of feature space and response variable, the 'randomForest' function was called with the default parameters of 500 trees in the forest, at least five units assigned per leaf in the tree, and the number of predictor variables p tested at each split in the tree as $p/3$ for regression and $\sqrt{p}$ for classification models. For convenience, the RF models used the 'out-of-bag' sample units for model validation rather than the leave-one-out cross validation employed for the kNN models. The R^2 value was calculated using the ensemble predictions for each regression model, as was the overall accuracy for each classification model.

3. Results

3.1. Image composites and harmonic regression

For the timeframe used in the study area, pixels in overlap zone 1 (both sidelap and endlap) of WRS-2 appeared in about 325–380 TM or ETM+ scenes, those in overlap zones 2 or 3 (either sidelap or endlap) in 215–265 scenes, and those in overlap zone 4 (no overlap) had 100–135 scenes, shown as an RGB image of the blue (R), NIR (G), and second SWIR (B) bands in Fig. 1. The pattern of high, medium, and low pixel values for scene totals depicted in the figure corresponds closely with the scene boundaries of WRS-2, indicating zones of overlap. These totals represent the largest possible pool of candidate observations that could be used to construct the composite images of TCT metrics. Observations either flagged as missing or scored as contaminated by snow or clouds were removed from this pool to produce a filtered pool of relatively clean observations.

Fig. 2 depicts the ratio of the filtered pool size to the total pool size for each reflective band as an RGB image, again showing the blue (R), NIR (G), and second SWIR (B) bands. Water bodies are clearly seen to have the smallest ratio values, meaning that most observations were removed by the snow or cloud filters. Another notable feature is the set of colored lines running parallel to the path of the satellite along the boundaries of overlap zone 4 in a

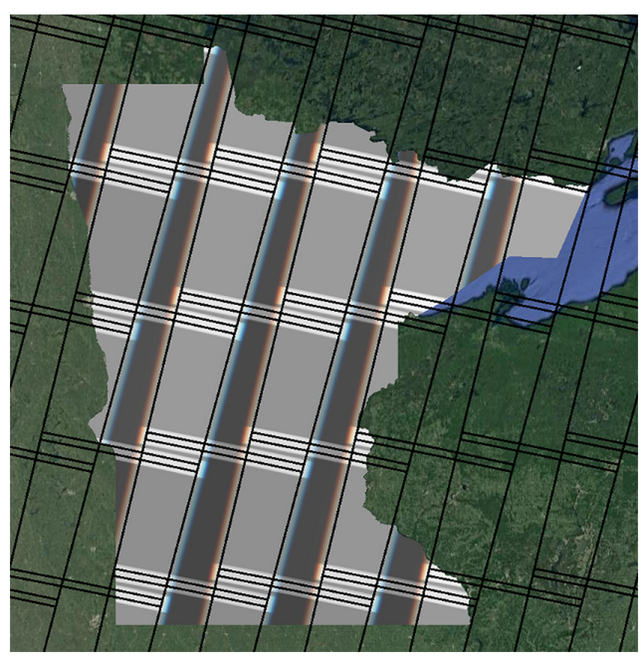

Fig. 1. RGB image of the total number of Landsat TM and ETM+ observations for each pixel in bands 1 (R), 4 (G), and 7 (B) for study timeframe, 2009–2013. Higher pixel values appear brighter. The black lines represent WRS-2 scene boundaries. Overlap zones are: (1) with both sidelap and endlap (white), (2) with sidelap (medium gray), (3) with endlap (intersection of dark gray and white), and (4) with neither sidelap nor endlap (dark gray).

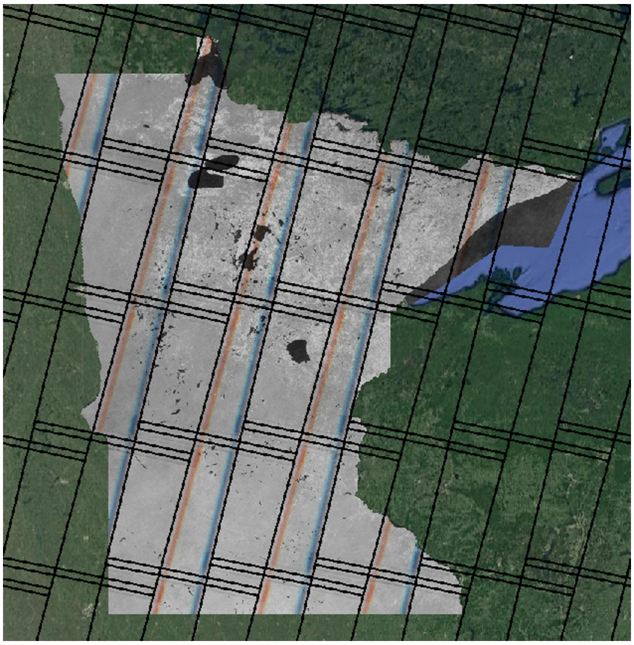

Fig. 2. RGB image of the ratio of the number of Landsat TM and ETM+ observations per pixel remaining after filtering out cloud and snow to the totals shown in Fig. 1 for bands 1 (R), 4 (G), and 7 (B). Higher pixel values appear brighter, ranging from 0% remaining after filtering (black) to 100% remaining (white). The black lines represent WRS-2 scene boundaries.

northeast-to-southwest orientation. These are caused by a differential across bands in data flagged as missing, and are also present yet less prominent in Fig. 1. Also visible is the pattern of higher-value white pixels among the intermediate-value gray pixels. Visual comparison of this pattern to finer resolution imagery suggests a strong correlation with tree cover, with pixels covered by tree canopy having higher pixel values. A final feature, barely visible at the scale of Fig. 2, is a pattern of alternating brighter and darker bands running perpendicular to the path of the satellite. This will be shown more clearly in the discussion in Fig. 9.

The filtered pool of observations for each band was used to construct 35 median value six-band composite images used for harmonic regression. Fig. 3 shows the OLS RMSE values as RGB images for TCT brightness (R), greenness (G), and wetness (B) for 1st order to 4th order Fourier series, with the values in each image stretched to a common range (i.e. the band ranges of the 1st order series) for visual comparison. All images show artifacts that correspond with the boundary between overlap zone 4 of WRS-2 and neighboring zones.

The corresponding mean, maximum, and minimum values for the study area are shown as bar charts in Fig. 4 to highlight the marginal improvement with increasing series order. GEE stores image assets at multiple spatial resolutions to facilitate efficient processing and display of geospatial data. Starting with the native spatial resolution, each subsequent scale (zoom level) differs by a factor of two. This means that pixel values at each coarser scale are assigned the mean of the four corresponding pixel values at the prior finer scale, e.g., 30-m spatial resolution pixels are aggregated to 60-m, 120-m, 240-m, 480-m, 940-m, and 1920-m spatial resolutions. The values in Fig. 4 were calculated using a pixel resolution of 1920 m for efficiency of display and show that mean RMSE for all TCT metrics decreased as the order of the series increased.

Fig. 5 shows the estimated OLS regression coefficients for the constant term, corresponding to the mean value, of the model for TCT brightness, greenness, and wetness as RGB images for 1st order to 4th order Fourier series, with the values in each image stretched to a common range for visual comparison. As was the case with Fig. 3, the images clearly show artifacts that correspond with the boundary between overlap zone 4 of WRS-2 and neighboring zones. Similar patterns appear in the images of the 1st order harmonic terms, which are present in all models, and are shown in Figs. 6 and 7. Comparable images for the 2nd order harmonic terms, which appear only in the 2nd through 4th order series, are shown in Fig. 8. Images for higher-order harmonic terms were created, but are not shown here.

3.2. Models of forest attributes using kNN and RF

The regression results for the *k*NN models are shown in Table 1. For each of the 8 continuous response variables, conditional on each of the feature spaces (i.e. composite vs. Fourier), R^2 in the table was estimated using the optimal value of k based on leave-one-out cross-validation. The values range from approximately 0.11 to 0.24 for the models using the composite feature space (designated ‘composite models’) and 0.31 to 0.55 for those using the Fourier feature space (designated ‘Fourier models’). The optimal value of k varied with both response variable and feature space used in the model, with it being considerably larger for the composite models (93–200) than for the Fourier models (22–69).

For each response variable, the ratio of the coefficients of determination using the two feature spaces is also shown, giving a measure of the gain in variance explained by the models using the estimated harmonic regression coefficients, indicating approximately two to three times greater explanatory power. The corresponding regression results for the RF models are shown in Table 2, exhibiting similar ranges for R^2 values and their ratios indicating approximately 2.5–3.5 times greater explanatory power of the Fourier models.

The classification results for the two-class *k*NN models are shown in the next set of tables. Table 3 shows the results for the composite model, with an overall accuracy of almost 82%, individual class accuracies of approximately 69–88%, and an optimal k of 33. Table 4 shows results for the Fourier model, with an overall accuracy of almost 93%, individual class accuracies of approximately 87–96%, and an optimal k of 12. The corresponding results for the two-class RF models are shown in Tables 5 and 6, indicating similar accuracies to the *k*NN models.

The classification results for the 8-class *k*NN models are shown in Tables 7 and 8, associated with the composite and Fourier models respectively. The composite model had an overall accuracy of almost 62%, individual class accuracies of approximately 41–74% (excluding the rarely sampled ‘grassland’ and ‘non-stocked forest’ classes), and an optimal k of eight. The Fourier model had an overall accuracy of approximately 81%, individual class accuracies of approximately 51–92% (again excluding the two rare classes), and an optimal k of nine. The corresponding results for the eight-class RF models are shown in Tables 9 and 10, indicating an improvement in overall and individual class accuracies similar to that shown in the *k*NN results for models using the estimated Fourier coefficients rather than the mean monthly composites.

4. Discussion

4.1. Image composites and harmonic regression

A few features shown in the first two figures merit some explanation. The visible mismatch between WRS-2 overlap zones and the regions of high, medium, and low pixel values shown in Fig. 1 is apparently due to the actual scene dimensions being slightly larger than the dimensions of the scene boundaries used

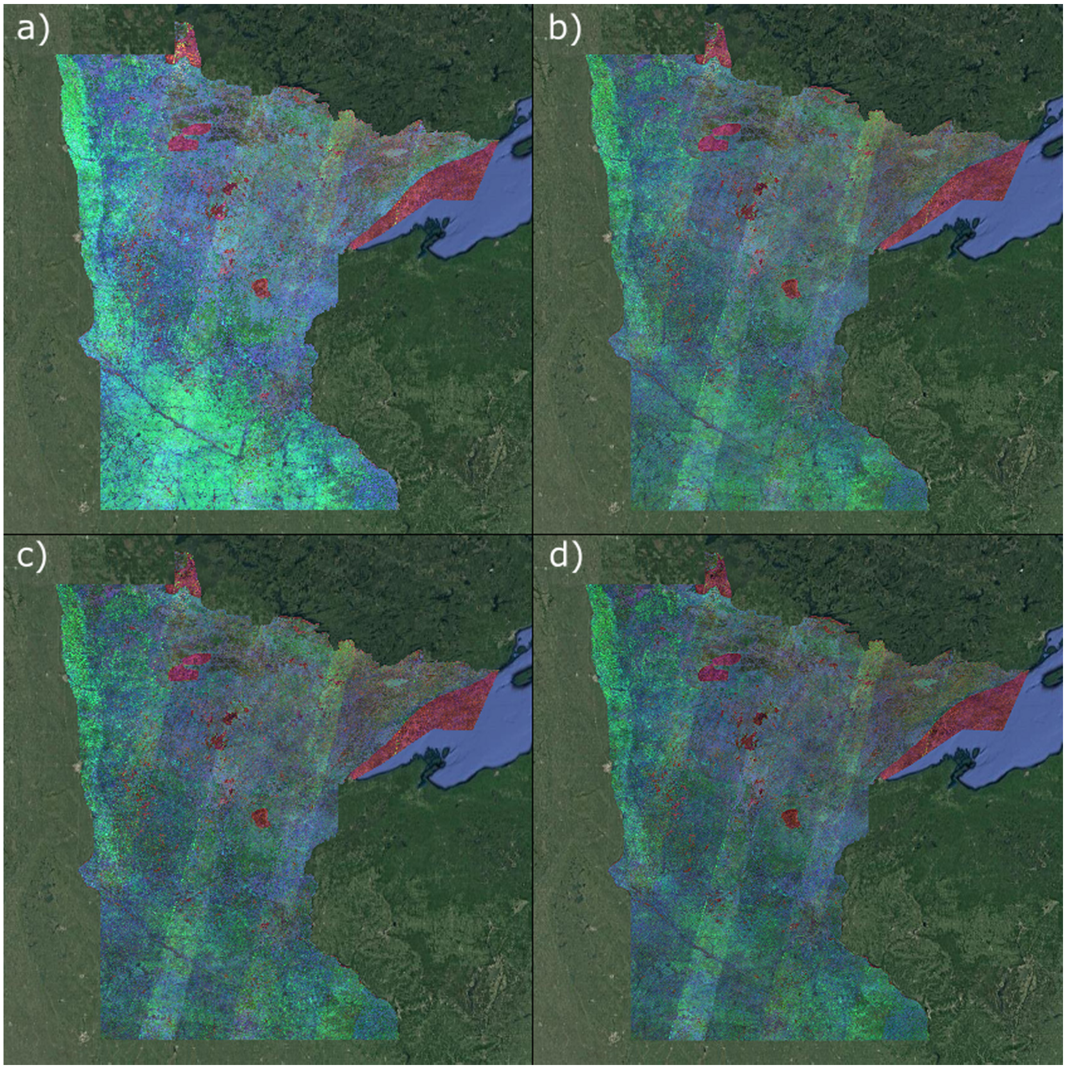

Fig. 3. Per-pixel RMSE values for 1st to 4th order Fourier series (a–d), displayed as RGB images of TCT brightness (R), greenness (G), and wetness (B). Larger RMSE values appear as brighter.

in the WRS-2 index map. This is simply noted and not considered problematic. However, the differential in the amount of data flagged as missing across bands near the zone 4 boundaries, visible in both Figs. 1 and 2, would have the effect of a differential reduction across bands in the pool of candidate observations for construction of composite images. This could result in spurious image artifacts, since each band composite image is calculated from a slightly different pool of observations.

Regarding the low values for water bodies in Fig. 2, Hall et al. (1995) stated that water bodies may have NDSI values in the range of snow, but lower NIR reflectance. Thus, most water pixels would also be filtered out by the snow filter. However, since the focus of this study is on NFI applications, differentiating water from snow was of secondary importance. Nevertheless, it is noted that the ratio image could be used to mask out water bodies from the study area if desired.

For the high value pixels in Fig. 2, it is obvious that fewer observations are filtered out for those pixels relative to others. One plausible explanation for the correlation between these pixels and those with tree canopy cover is that snow falling on trees, with or without foliage, does not remain in situ as long as snow falling on the land surface. This result supports the findings of Stueve et al. (2011), who demonstrated the use of snow-covered Landsat time series imagery to improve the mapping of forest disturbances. However, the focus of this study is on the development of methods that can be applied across the US using NFI data, even where snow cover may be rare or non-existent. Therefore, this feature was not used as auxiliary data for the modeling of forest attributes from NFI data.

The alternating bands of brighter and darker pixels, visible in some regions of the study area, appear to be caused by the presence of SLC-off data gaps. Fig. 9(a) is a subset of Fig. 2 depicted at a finer scale that clearly illustrates this alternating pattern. The bands are not visible in overlap zone 4, bounded by red pixels on the western edge and blue pixels on the eastern edge. They are clearly visible in overlap zone 2, with blue pixels on the western edge and red pixels on the eastern edge. These artifacts are periodic in nature in the spatial domain. Therefore, a power spectrum of these spatial characteristics of the image can be estimated via a Fast Fourier Transform (FFT).

Fig. 9(b) shows the power spectrum of the image in (a), using the ImageJ image processing and analysis software (Abràmoff et al., 2004). Periodic features in the spatial domain appear as bright spots, seen in the bottom half, with lower frequency features being closest to the center. The direction of the vector from the center of the power spectrum to the feature corresponds with

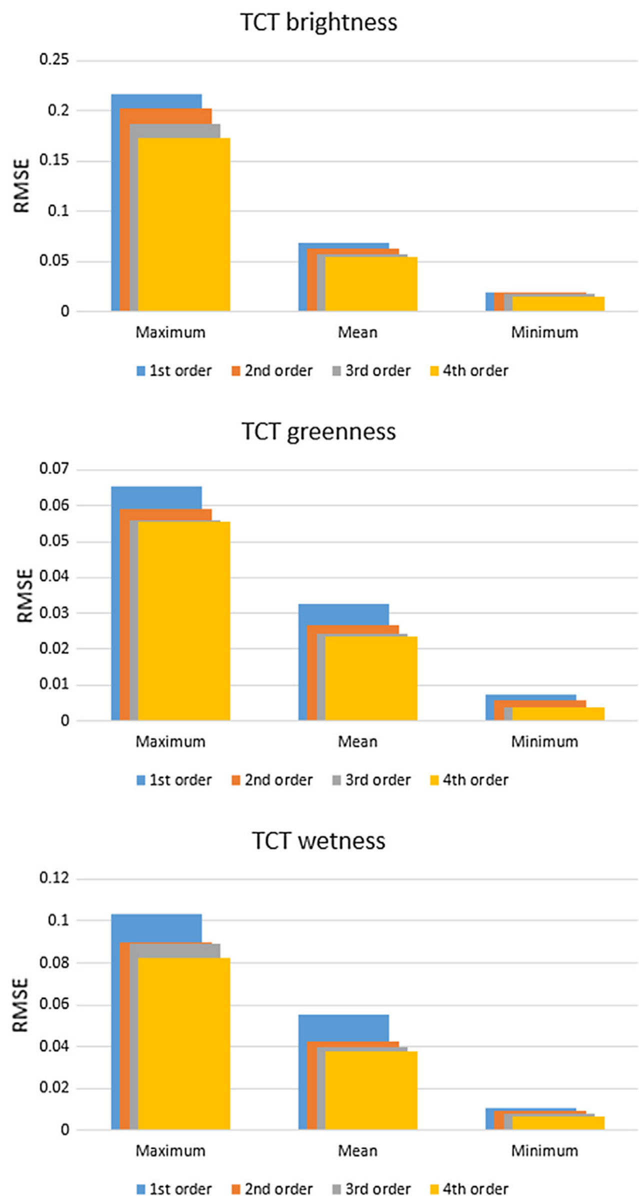

Fig. 4. Bar charts of maximum, mean, and minimum RMSE for TCT metrics, summarized for the study area from the pixel values in Fig. 3.

the direction of the spatial pattern in the original image. Because the power spectrum is symmetrical about the center, only half of these features need to be masked, as shown in the top half. By using the corresponding inverse FFT on the masked power spectrum, the spatial artifacts can be filtered from the original image.

Fig. 9(c) shows the difference between the original and filtered images, with larger differences appearing as brighter pixels. The difference image clearly shows that the largest differences, due to the periodic spatial patterns induced by the SLC-off gaps, occur primarily in overlap zone 2 and are mostly absent in overlap zone 4. It is not immediately clear whether similar results would be found in a comparable analysis of the images in Fig. 3 or 5–8.

The images in Fig. 3 show that much of the improvement in fit with increasing series order for greenness and wetness appears to be for cropland pixels (in cyan), which have much larger RMSE values for these two metrics than other pixels in the 1st order image. Improvement in the fit for brightness appears to be uniformly distributed across the study area, with RMSE for brightness remaining much larger than RMSE for greenness and wetness for water pixels (in red). This is to be expected, since overall scene luminance is typically the largest source of variability across an image. Likewise, the aggregate study area RMSE values depicted in the graphs in Fig. 4 show that greenness and wetness improved only marginally beyond the 2nd order, while brightness exhibited steady improvement with increasing series order. Similar results are seen for maximum values, while the results for minimum values are similar only for brightness and greenness. Minimum wetness exhibited steady improvement with increasing series order.

Fig. 10(a) shows a subset of the 3rd order image in Fig. 3, displayed at a finer scale. Fig. 10(b) and (c) show the results a power spectrum analysis comparable to what was done in Fig. 9. The difference image suggests that the artifacts caused by the SLC-off gaps in the composite images of TCT metrics are also present in the images generated from the harmonic regression procedure. Furthermore, these artifacts are again most visible in overlap zone 2.

Based on the landscape patterns seen in Figs. 5–8, harmonic regression of time series of Landsat imagery captures information that is correlated with known historical land cover patterns throughout the state. In the case of Fig. 5, croplands correspond well with pixels appearing along the color spectrum from yellow to brown, while forest land corresponds with the spectrum from cyan to light purple. Other land cover types, such as developed land (urban areas) and water bodies, also correspond to distinctive spectral patterns in the image. This correspondence holds, though perhaps to a lesser degree, for the higher order images as well.

The cloud and snow filters effectively remove most observations contaminated by clouds and snow. Yet, there remain some visible image artifacts regardless of series order, as noted in the results for Fig. 3. The image artifacts are less noticeable for forest land pixels with increasing series order. However, the opposite effect is noted for some water and cropland pixels. Closer examination of these artifacts at finer scales suggests that they are also associated with SLC-off gaps that fall on cropland or water pixels.

Fig. 11 shows a small subset of Fig. 5, which includes a boundary between overlap zones 2 and 4 (i.e. zones with only sidelap and no overlap, respectively). The SLC-off artifacts become faintly visible in the 3rd order image, but are clearly visible in the 4th order image. The artifacts are present only in overlap zone 2, on the left-hand side of each image in the figure. Further examination across the study area at finer scales indicates that these artifacts are also present in overlap zone 4, but generally only for water pixels, or for cropland pixels that fall within the areas of differential missing data across bands seen as colored lines in Figs. 1 and 2.

It is suggested here that these SLC-off artifacts are due to the composite images being constructed from different pools of observations for neighboring pixels in areas affected by the SLC failure, leading to discontinuities in the resultant harmonic regression coefficient images. In the case of the study area of Minnesota, located at northerly latitudes, the issue is mitigated to some degree by the width of overlap zone 2 (those areas with sidelap). The further north a Landsat scene is located, the more sidelap there is with adjacent scenes, and the greater the likelihood that an SLC-off gap will be filled by a pixel observation from another scene.

While these artifacts are clearly visible in the higher order images of the Fourier series coefficients, they are less conspicuous in the lower order images. This is particularly noticeable for SLC-off gaps falling on cropland and water pixels. This result, along with the results presented in Figs. 3 and 4, suggests that higher order harmonics of the 3rd and 4th order series are fitting extraneous noise rather than meaningful signal, i.e. the spurious oscillations noted in earlier studies. In the case of water pixels, the noise is likely the result of specular reflectance, from the mirror-like surface of calm water bodies, which varies with the view angle of the sensor. In the case of croplands, the noise is likely due to

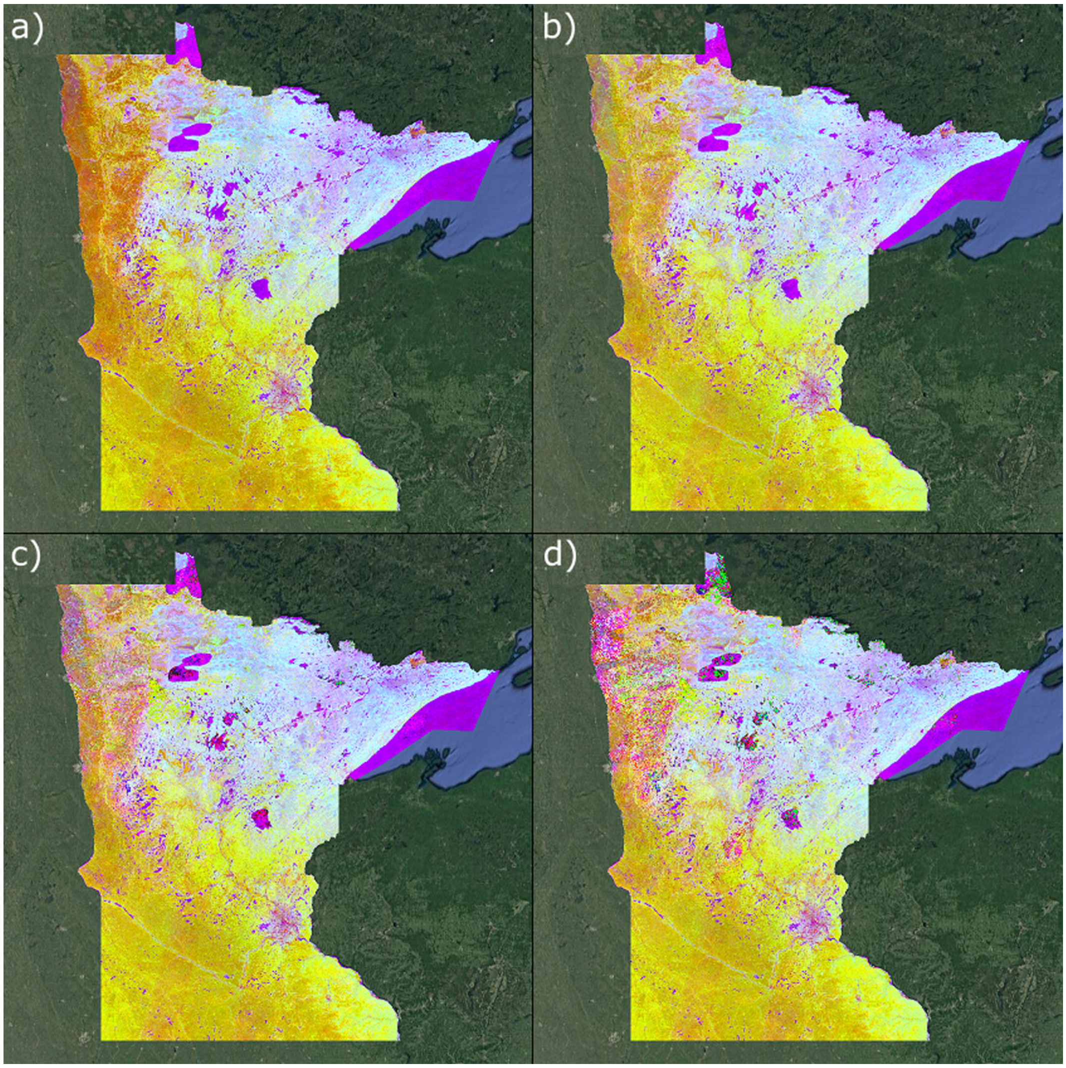

Fig. 5. RGB images of mean TCT brightness (R), greenness (G), and wetness (B), estimated from 1st to 4th order Fourier series (a–d).

variable cropping patterns from year to year. Since the harmonic regression was conducted on composite images constructed from data collected over the study timeframe (five years), many cropland pixels will not exhibit regular periodic behavior because of crop rotation.

As was done earlier in Figs. 9 and 10, a power spectrum analysis could be used, along with the corresponding inverse FFT, to correct these spatial artifacts. However, that process would involve a considerable amount of image interpretation and manipulation of the power spectrum image by the analyst that would be difficult to automate over large areas. More important, it is not immediately clear whether these artifacts would necessarily cause similar results in maps of forest attributes developed from the *k*NN and RF models. For these reasons, the spatial FFT correction was left for a future study. As a more efficient means of mitigating the potential impacts of these artifacts, the uncorrected 3rd order images were selected for use as auxiliary data for the modeling of forest attributes from NFI data.

4.2. Models of forest attributes using kNN and RF

There are a few observations to note in the results of the regression models shown in Tables 1 and 2. For both *k*NN and RF modeling approaches, the Fourier models demonstrated marked improvement over the composite models, in terms of the ratios of coefficients of determination. Also noted for the *k*NN Fourier models, regardless of the response variable, R^2 increased while the optimal value of k decreased relative to the composite models. This means that as the correlation between the predictor and response variables increased, the predicted values were based on fewer neighbors, suggesting they were more local in terms of the feature space of predictor variables.

Another interesting result for all regression models, regardless of modeling approach or predictor feature space, is that R^2 values for those models using the response variables for only live broadleaf trees (broadleaf tree models) were all smaller than the corresponding models for all live trees (all tree models). While one might expect this result, it is notable that the ratios for the broadleaf tree models are all larger than those of the corresponding all tree models. The larger relative improvement in the broadleaf tree models, as measured by the ratios of the coefficients of determination, suggests that estimated Fourier coefficients enable differentiation between broadleaf and coniferous trees.

The classification models show a similar pattern of results for both the *k*NN and RF modeling approaches. For the results of the two-class models, shown in Tables 3–6, there is improvement in overall accuracy of approximately 11 percentage points in the Fourier models relative to the composite models. For the

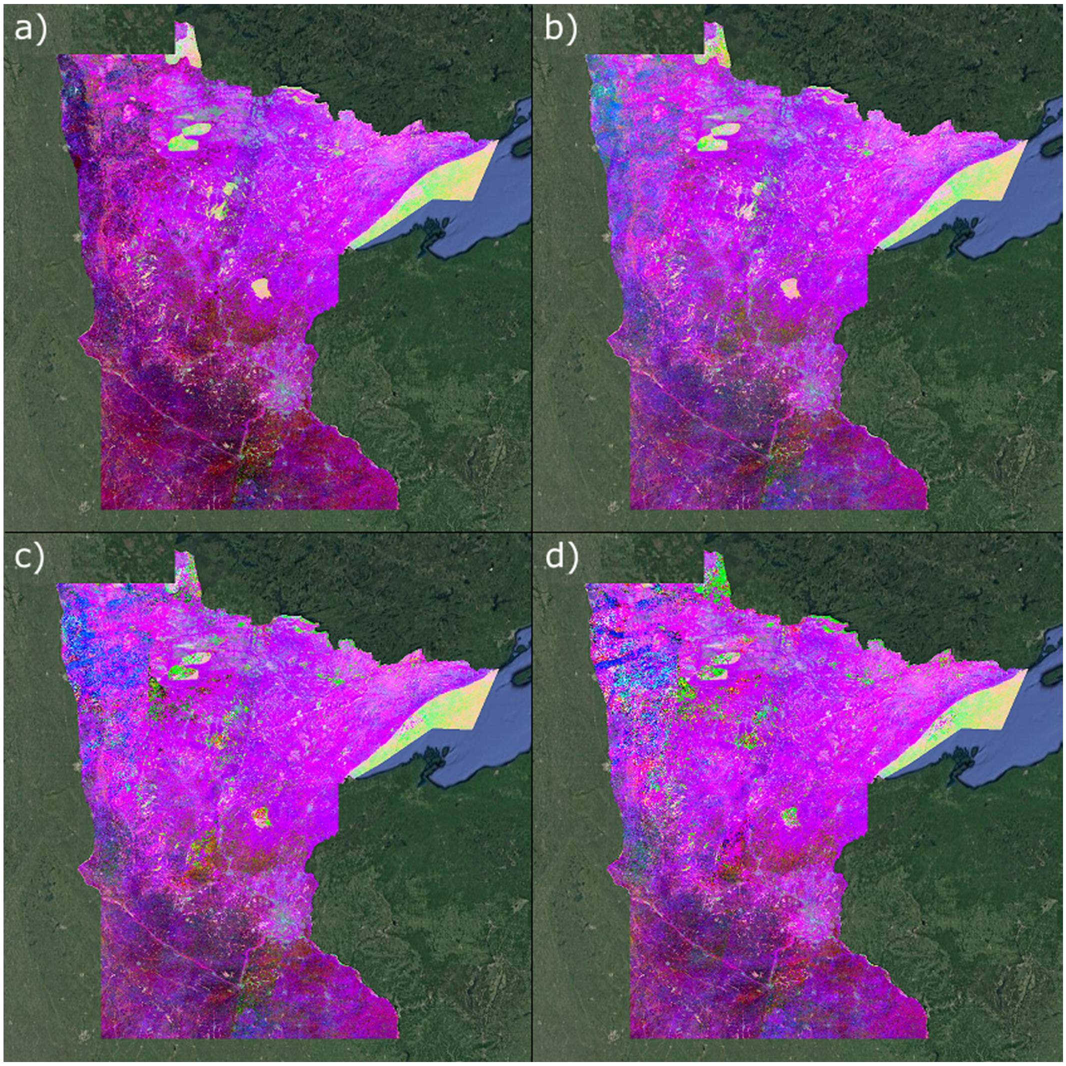

Fig. 6. RGB images of the coefficient of the cosine term of the 1st harmonic for TCT brightness (R), greenness (G), and wetness (B), estimated from 1st to 4th order Fourier series (a–d).

eight-class models, the improvement in overall accuracy amounts to almost 20 percentage points. Interestingly for the *k*NN models, while the two-class case saw a substantial decrease in the optimal value of *k* (33 vs. 12) when using the Fourier rather than composite models, the eight-class case showed essentially no difference (eight vs. nine).

Regardless of modeling approach or feature space used, for the two-class models the class accuracies (both producer's and user's accuracy) were greater for the 'non-forest' class than the 'forest' class. It also should be noted that there were 12,013 'non-forest' units in the reference set vs. 5330 'forest' units, so it would be expected that even by random assignment the 'non-forest' class would have the greater class accuracy. The 'non-forest' class accuracies were approximately 7–11% greater, while the 'forest' class accuracies were approximately 22–32% greater using the Fourier models relative to the composite models.

For the eight-class models, the individual class results shown in Tables 7-10 are less straightforward to summarize. Using the composite feature space with both the *k*NN and RF approaches, the 'cropland' class had the greatest accuracies by a substantial margin, followed by the 'broadleaf forest', 'coniferous forest', and 'water' classes. Using the Fourier feature space with both the *k*NN and RF approaches, the class results differ depending on whether producer's or user's accuracies are considered. Based on producer's accuracy, the 'cropland' class again had the greatest accuracy, followed closely by the 'water' and 'broadleaf forest' classes, then the 'coniferous forest' class. Based on user's accuracy, the 'water' class had the greatest accuracy, followed closely by the 'cropland' class, then the 'broadleaf forest' and 'coniferous forest' classes.

Regardless of the modeling approach and feature space used, the rarely sampled 'grassland' and 'non-stocked forest' classes had the lowest classification accuracies of all classes, with no reference units being correctly classified. The results for the 'settlement' and 'wetland' classes were mixed, with intermediate accuracies. Using the composite feature space with both the *k*NN and RF approaches, these classes had greater user's accuracies than producer's accuracies, with the 'settlement' class showing slightly greater accuracies than the 'wetland' class. The same pattern holds for the Fourier models.

All classes showed greater individual producer's and user's accuracies using the Fourier models rather than the composite models, some markedly so. The pattern of improvement was consistent, whether using the *k*NN or RF modeling approaches. Relative to the class accuracies achieved using the composite models, the Fourier models showed improvements ranging from approximately 10–20% for the 'cropland' class, 35–70% for the two stocked

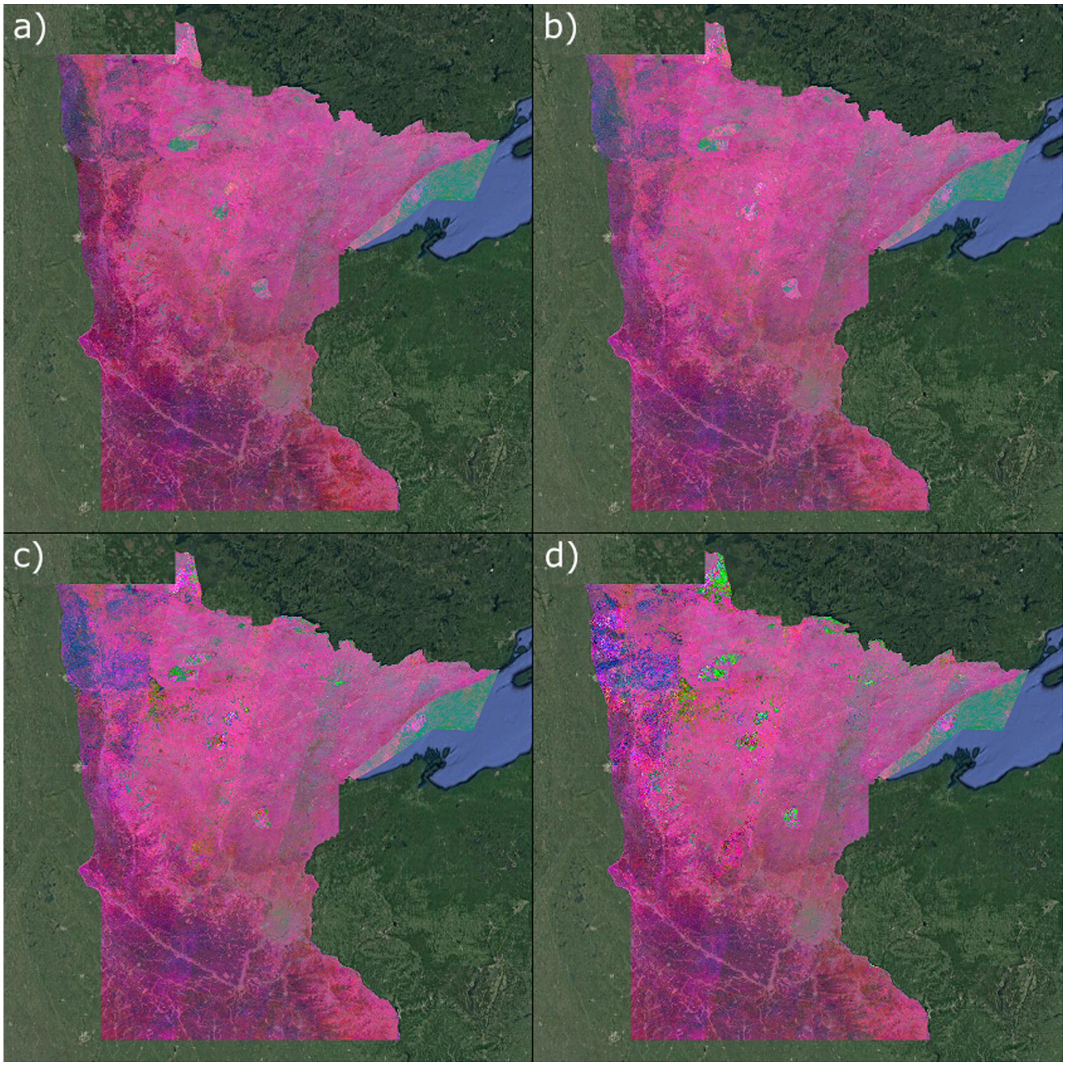

Fig. 7. RGB images of the coefficient of the sine term of the 1st harmonic for TCT brightness (R), greenness (G), and wetness (B), estimated from 1st to 4th order Fourier series (a–d).

forest classes, 40–165% for the 'settlement' class, 85–150% for the 'water' class, and 85–370% for 'wetland' class.

Although it was not a formal objective of the study, it should be noted that on balance the RF models produced slightly greater R^2 values and classification accuracies than the comparable *k*NN models, though this was not universally true. For the regression models using the composite feature space, the *k*NN models resulted in R^2 values that were marginally greater than those of the corresponding RF models. However, the converse was true for all regression models using the Fourier feature space. From the perspective of comparing modeling approaches, the classification results were once again less straightforward. For the two-class models using either the composite or Fourier feature space, the overall accuracies were nearly identical and there were no clear patterns in the individual class results. For the 8-class models, the overall accuracies were approximately one to two percentage points better using the RF approach. For the composite models using the RF approach, the user's accuracies of almost all classes were at least marginally greater than the class results using the *k*NN approach. The corresponding producer's accuracies were less conclusive. A similar pattern can be seen in the results for the eight-class Fourier models. It is possible that even these small differences between the two modeling approaches may become negligible with additional optimization of the *k*NN models, particularly through the use feature selection or feature weighting during development of the feature space of predictor variables.

The objective of the study was to compare alternative feature spaces derived from dense Landsat time series imagery, and not necessarily to produce the best possible models under either alternative. However, even without extensive efforts at optimization of the *k*NN models, the results compare favorably with similar earlier studies. McRoberts (2009b) used the *k*NN algorithm with data collected on FIA sub-plots and 12 spectral features derived from multi-date TM and ETM+ imagery to predict tree volume, density, and basal area for a study area in Northern Minnesota corresponding to WRS-2 Path 27 Row 27. The mean R^2 value for all three models was 0.11 using individual sub-plots and pixels, and 0.24 when aggregating FIA observations to the plot level and using a 3×3 pixel about each plot center. Likewise, the 3-class (non-forest, coniferous forest, and broadleaf forest) and 4-class (non-forest, coniferous forest, broadleaf forest, and mixed forest) classification models had overall accuracies of 72% and 65% respectively, with individual class accuracies ranging from 62–91% and 10–89% respectively. McRoberts (2012), in a study using the same set of predictor and response variables for the same study area as the 2009 study, determined that the optimal value of *k* that minimized

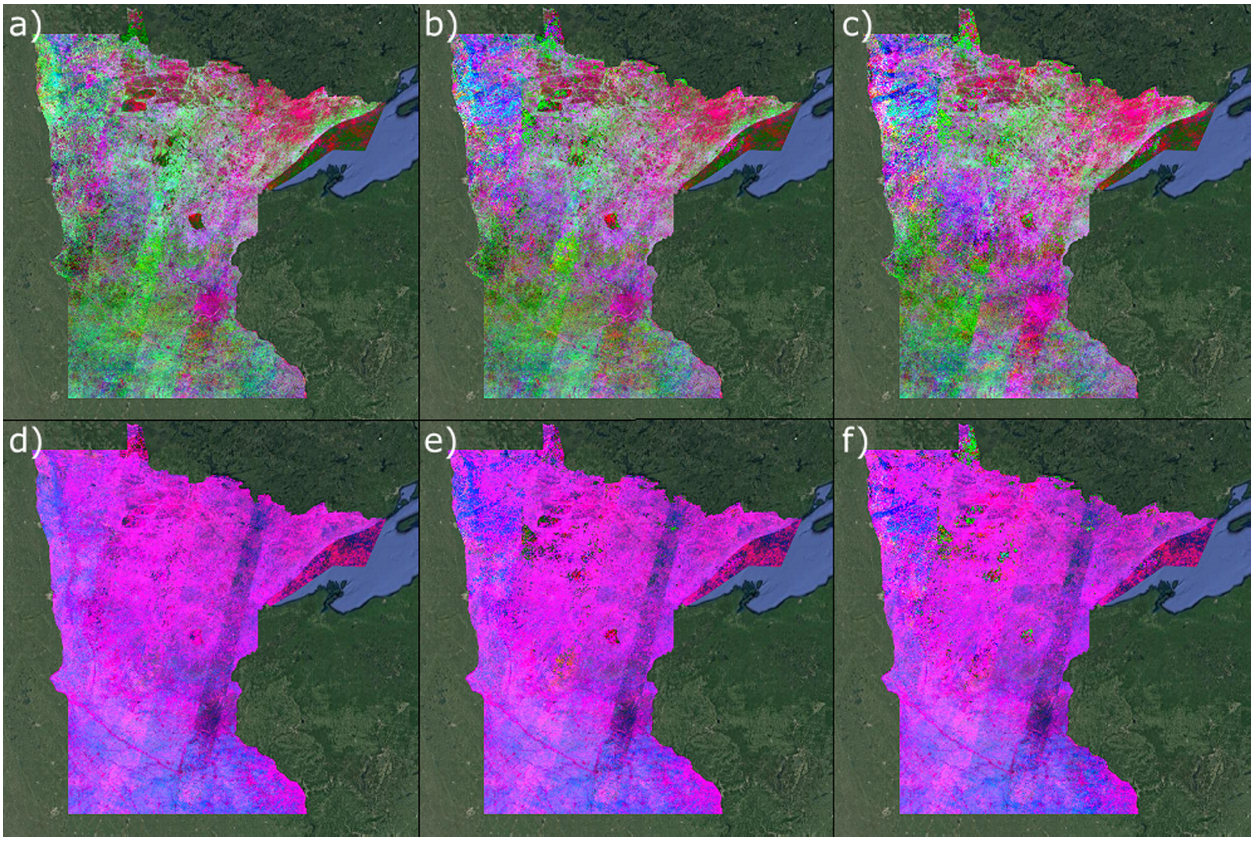

Fig. 8. RGB images of the coefficients of the cosine (a–c) and sine (d–f) terms of the 2nd harmonic for TCT brightness (R), greenness (G), and wetness (B), estimated from 2nd to 4th order Fourier series.

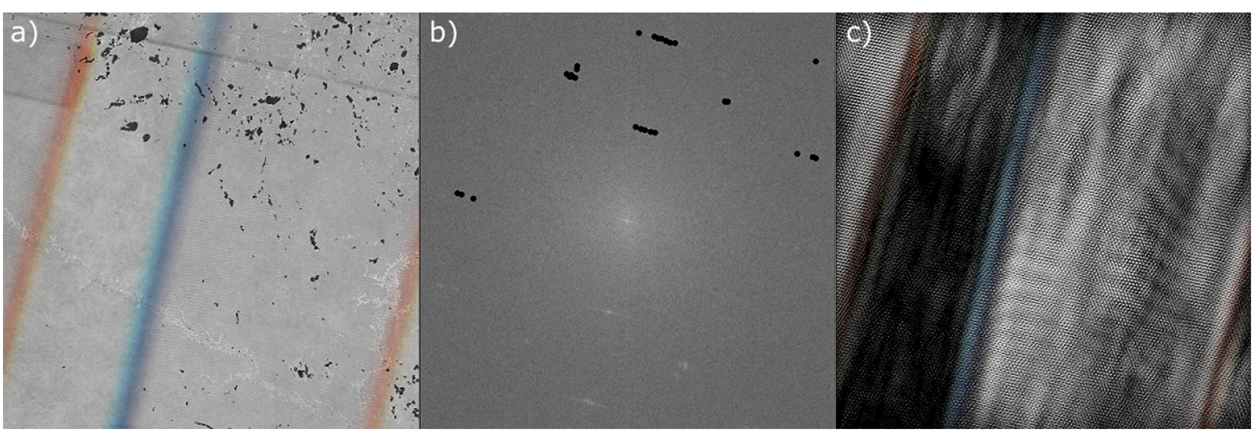

Fig. 9. (a) Subset of Fig. 2, (b) its power spectrum showing masked artifacts in black, and (c) the difference between the original and filtered images, with larger differences appearing brighter.

Table 1
Results of the *k*NN regression models of the number (trees), basal area (barea), foliage biomass (biofol), and total aboveground biomass (bioall) of all live trees on the central subplot, as well as comparable values for only live broadleaf trees (_bl). Results include the mean of the observations ($\overline{Y}$) and root mean square error (RMSE) of the predictions, as well as the coefficient of determination (R^2) for models using the composite and Fourier feature spaces, their ratio (Fourier/composite), and the optimal value of *k* based on leave-one-out cross-validation.

*k*NN	$\overline{Y}$	RMSE comp.	RMSE Fourier	R^2 comp.	R^2 Fourier	R^2 ratio	Optimal *k* comp.	Optimal *k* Fourier
trees (#/ha)	62.64	144.2	127.1	0.1658	0.3517	2.122	116	37
trees_bl (#/ha)	40.76	119.6	105.2	0.1103	0.3129	2.837	200	69
barea (m^2/ha)	1.427	2.580	2.004	0.2287	0.5364	2.345	134	29
barea_bl (m^2/ha)	0.9316	2.123	1.681	0.1618	0.4759	2.941	192	47
biofol (kg/ha)	253.5	492.2	377.8	0.2381	0.5517	2.317	93	22
biofol_bl (kg/ha)	119.8	282.2	226.9	0.1537	0.4545	2.957	134	64
bioall (kg/ha)	4824	10,070	8294	0.1739	0.4410	2.535	134	64
bioall_bl (kg/ha)	3537	9134	7556	0.1339	0.4090	3.054	143	64

Table 2
Results of the RF regression models of the number (trees), basal area (barea), foliage biomass (biofol), and total aboveground biomass (bioall) of all live trees on the central sub-plot, as well as comparable values for only live broadleaf trees (_bl). Results include the mean of the observations ($\overline{Y}$) and root mean square error (RMSE) of the predictions, as well as the coefficient of determination (R^2) for models using the composite and Fourier feature spaces and their ratio (Fourier/composite).

RF	$\overline{Y}$	RMSE comp.	RMSE Fourier	R^2 comp.	R^2 Fourier	R^2 ratio
trees (#/ha)	62.64	145.8	124.9	0.1544	0.3742	2.424
trees_bl (#/ha)	40.76	121.0	104.0	0.09884	0.3281	3.319
barea (m^2/ha)	1.427	2.603	1.958	0.2181	0.5561	2.549
barea_bl (m^2/ha)	0.9316	2.149	1.655	0.1476	0.4906	3.324
biofol (kg/ha)	253.5	496.4	367.6	0.2284	0.5750	2.517
biofol_bl (kg/ha)	119.8	285.9	223.7	0.1378	0.4686	3.399
bioall (kg/ha)	4824	10,190	8178	0.1606	0.4556	2.837
bioall_bl (kg/ha)	3537	9255	7454	0.1193	0.4234	3.548

Table 3
Results of the two-class *k*NN classification model using the composite feature space. Results include the optimal value of *k* based on leave-one-out cross-validation, number of reference units assigned to each class, individual class user's (commission error) and producer's (omission error) accuracies, as well as overall accuracy.

*k*NN composite (optimal *k* = 33)		Predicted			
		Non-forest	Forest	Total	Producer's accuracy
Observed	Non-forest	10,521	1492	12,013	87.58%
	Forest	1637	3693	5330	69.29%
	Total	12,158	5185	17,343	
	User's accuracy	86.54%	71.22%		81.96%

Table 4
Results of the two-class *k*NN classification model using the Fourier feature space. Results include the optimal value of *k* based on leave-one-out cross-validation, number of reference units assigned to each class, individual class user's (commission error) and producer's (omission error) accuracies, as well as overall accuracy.

*k*NN Fourier (optimal *k* = 12)		Predicted			
		Non-forest	Forest	Total	Producer's accuracy
Observed	Non-forest	11,267	746	12,013	93.79%
	Forest	500	4830	5330	90.62%
	Total	11,767	5576	17,343	
	User's accuracy	95.75%	86.62%		92.82%

Table 5
Results of the two-class RF classification model using the composite feature space. Results include the number of reference units assigned to each class, individual class user's (commission error) and producer's (omission error) accuracies, as well as overall accuracy.

RF composite		Predicted			
		Non-forest	Forest	Total	Producer's accuracy
Observed	Non-forest	10,648	1365	12,013	88.64%
	Forest	1759	3571	5330	67.00%
	Total	12,407	4936	17,343	
	User's accuracy	85.82%	72.35%		81.99%

Table 6
Results of the two-class RF classification model using the Fourier feature space. Results include the number of reference units assigned to each class, individual class user's (commission error) and producer's (omission error) accuracies, as well as overall accuracy.

RF Fourier		Predicted			
		Non-forest	Forest	Total	Producer's accuracy
Observed	Non-forest	11,437	576	12,013	95.21%
	Forest	609	4721	5330	88.57%
	Total	12,046	5297	17,343	
	User's accuracy	94.94%	89.13%		93.17%

RMSE for tree volume models was 25 with a feature space consisting of a subset of 6 of the original 12 spectral features.

The RF regression model results are also comparable to those from an earlier study using FIA data and Landsat time series imagery. Zhu and Liu (2015) conducted a study in southeast Ohio for mapping and estimation of live tree aboveground biomass. The study used measurements from all sub-plots on a subset of 161 homogeneous FIA plots from a predominantly high biomass (over 100 metric tons/ha) 11-county study area, along with terrain-corrected NDVI values derived from six cloud-free Landsat scenes

Table 7
Results of the eight-class *k*NN classification model using the composite feature space. Results include the optimal value of *k* based on leave-one-out cross-validation, number of reference units assigned to each class, individual class user's (commission error) and producer's (omission error) accuracies, as well as overall accuracy.

*k*NN composite (optimal $k = 8$)		Predicted									
		Water	Crop.	Grass.	Settle.	Wet.	Conif.	Broad.	Non.	Total	Prod. Acc.
Observed	Water	347	275	0	18	48	74	239	0	1001	34.67%
	Crop.	121	7209	0	149	190	115	661	0	8445	85.36%
	Grass.	0	19	0	1	3	0	5	0	28	0.00%
	Settle.	27	568	1	213	31	52	177	0	1069	19.93%
	Wet.	58	668	0	31	190	107	416	0	1470	12.93%
	Conif.	58	197	0	19	78	631	536	0	1519	41.54%
	Broad.	135	825	0	87	178	381	2150	1	3757	57.23%
	Non.	4	12	0	2	9	4	23	0	54	0.00%
	Total	750	9773	1	520	727	1364	4207	1	17,343	
	User. Acc.	46.27%	73.76%	0.00%	40.96%	26.13%	46.26%	51.11%	0.00%		61.93%

Table 8
Results of the eight-class *k*NN classification model using the Fourier feature space. Results include the optimal value of *k* based on leave-one-out cross-validation, number of reference units assigned to each class, individual class user's (commission error) and producer's (omission error) accuracies, as well as overall accuracy.

*k*NN Fourier (optimal $k = 9$)		Predicted									
		Water	Crop.	Grass.	Settle.	Wet.	Conif.	Broad.	Non.	Total	Prod. Acc.
Observed	Water	853	14	0	13	50	35	36	0	1001	85.21%
	Crop.	7	7986	1	119	171	4	157	0	8445	94.56%
	Grass.	0	19	0	1	5	0	3	0	28	0.00%
	Settle.	15	340	0	430	76	35	173	0	1069	40.02%
	Wet.	41	405	0	49	549	91	335	0	1470	37.35%
	Conif.	6	15	0	12	68	1079	338	1	1519	71.03%
	Broad.	8	157	0	39	144	220	3189	0	3757	84.88%
	Non.	0	6	0	2	6	8	32	0	54	0.00%
	Total	930	8942	1	665	1069	1472	4263	1	17,343	
	User. Acc.	91.72%	89.31%	0.00%	64.66%	51.36%	73.30%	74.81%	0.00%		81.22%

Table 9
Results of the eight-class RF classification model using the composite feature space. Results include the number of reference units assigned to each class, individual class user's (commission error) and producer's (omission error) accuracies, as well as overall accuracy.

RF composite		Predicted									
		Water	Crop.	Grass.	Settle.	Wet.	Conif.	Broad.	Non.	Total	Prod. Acc.
Observed	Water	409	262	0	9	20	66	235	0	1001	40.86%
	Crop.	137	7473	0	57	67	73	638	0	8445	88.49%
	Grass.	0	23	0	0	0	0	5	0	28	0.00%
	Settle.	39	606	0	152	11	44	207	0	1069	14.22%
	Wet.	58	752	0	16	111	106	427	0	1470	7.55%
	Conif.	51	193	0	5	45	663	562	0	1519	43.65%
	Broad.	138	822	0	27	81	317	2372	0	3757	63.14%
	Non.	2	16	0	1	4	7	24	0	54	0.00%
	Total	834	10,157	0	267	339	1276	4470	0	17,343	
	User. Acc.	49.04%	73.57%	NA	56.93%	32.74%	51.96%	53.06%	NA		64.46%

Table 10
Results of the eight-class RF classification model using the Fourier feature space. Results include the number of reference units assigned to each class, individual class user's (commission error) and producer's (omission error) accuracies, as well as overall accuracy.

RF Fourier		Predicted									
		Water	Crop.	Grass.	Settle.	Wet.	Conif.	Broad.	Non.	Total	Prod. Acc.
Observed	Water	884	18	0	3	45	16	35	0	1001	88.31%
	Crop.	7	8180	0	48	67	0	143	0	8445	96.86%
	Grass.	0	20	0	1	3	0	4	0	28	0.00%
	Settle.	24	405	0	403	55	37	145	0	1069	37.70%
	Wet.	47	500	0	18	520	71	314	0	1470	35.37%
	Conif.	7	25	0	12	56	1121	298	0	1519	73.80%
	Broad.	7	199	0	22	106	213	3210	0	3757	85.44%
	Non.	0	10	0	1	7	5	31	0	54	0.00%
	Total	976	9357	0	508	859	1463	4180	0	17,343	
	User. Acc.	90.57%	87.42%	NA	79.33%	60.54%	76.62%	76.79%	NA		82.56%

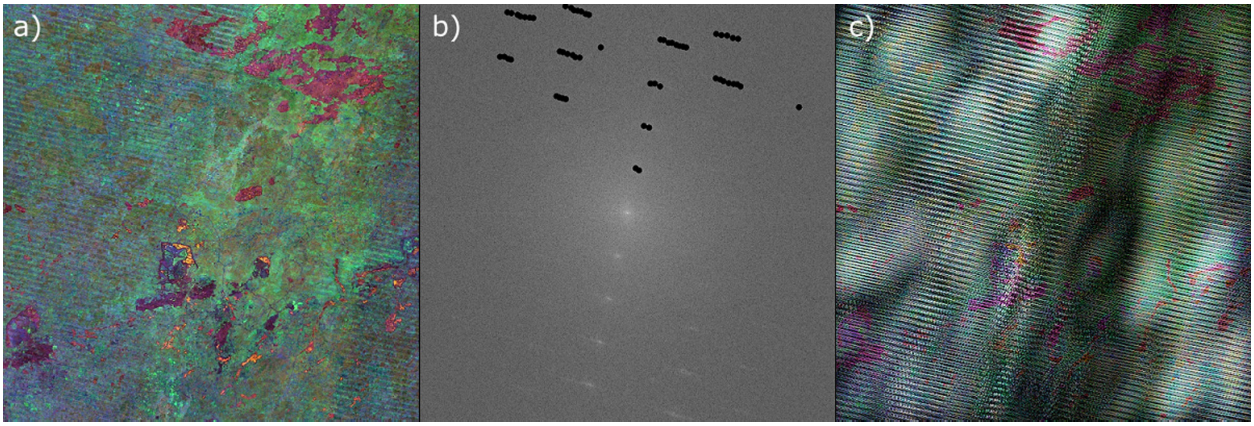

Fig. 10. (a) Subset of the 3rd order image in Fig. 3, (b) its power spectrum showing masked artifacts in black, and (c) the difference between the original and filtered images, with larger differences appearing brighter.

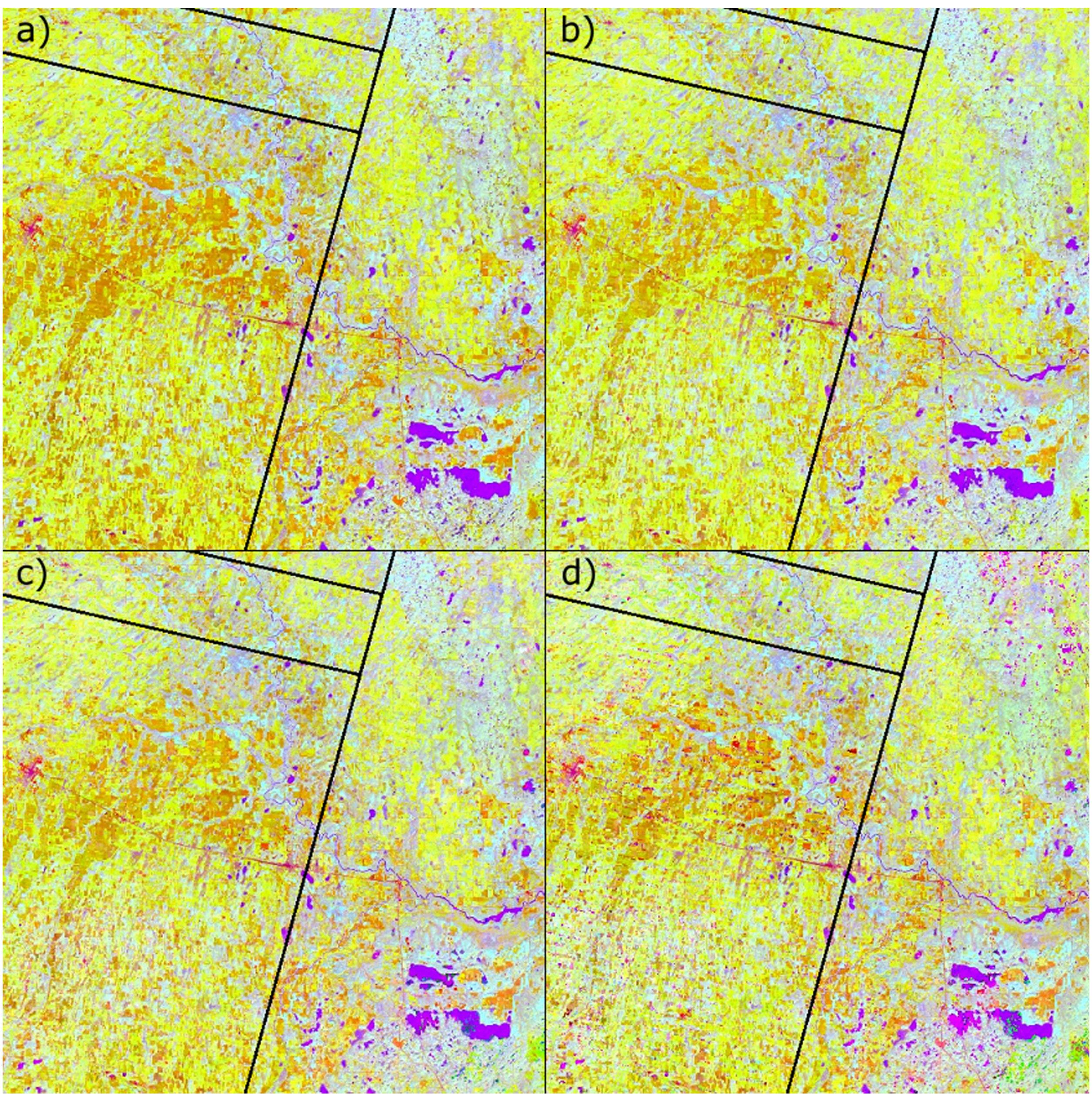

Fig. 11. Subset of the 1st to 4th order (a–d) images in Fig. 5. The black lines represent WRS-2 scene boundaries.

from one growing season. Predictions were made using six modeling methods, with R^2 values ranging from 0.48 for RF to 0.54 for artificial neural networks.

5. Conclusions

There are a number of conclusions to be drawn from this study. First, harmonic regression using Fourier series fitted to composite images derived from dense time series of Landsat imagery was shown to be an effective means of handling missing data in the imagery due to the presence of clouds and snow. Second, the artifacts in the ETM+ image record due the SLC-off condition were mitigated to a great extent both through supplementation with concurrent TM imagery during compositing and by use of a low-order Fourier series. Third, and most important, the estimated Fourier coefficients developed by harmonic regression of TCT time series were correlated with land cover, including tree cover, based on a qualitative assessment of the imagery and knowledge of land cover patterns in the study area.

The strength of this correlation was quantifiably demonstrated using two non-parametric modeling approaches and a range of response variables derived from NFI data. Regression models using a feature space of estimated Fourier coefficients showed a two- to three-fold increase in explained variance for a small set of continuous response variables, relative to comparable models using monthly image composites. Similarly, the overall accuracies of the two-class and eight-class classification models using the Fourier feature space were approximately 10–20 percentage points higher than the models using the composite feature space. The corresponding individual class accuracies likewise were approximately six to 21 percentage points higher in the two-class case and 10–45 percentage points higher in the eight-class case when using the Fourier coefficients versus the composite images as predictor variables.

The ultimate utility of this study relates to the role that these models might play in improving the precision of population estimates of land cover and forest attributes. Comprehensive national forest inventories, such as the one conducted by FIA in the US, are expensive by nature. In order to collect the information used in this study, particularly the continuous response variables, field crews had to travel to and make tree measurements on each of the forested plots used in the analysis, amounting to approximately 6000 plots in this case. This represents a substantial investment by the US Forest Service. Yet, even at the FIA sampling intensity of one plot per 2400 ha, the sample size required for reliable estimation would limit the application of most design-based methods to geographic areas, or populations, that are on the order of multiple counties within a state. By incorporating models such as the ones used in this study into model-assisted or model-based approaches, the scale of application of FIA data could approach what is needed for tactical forest management decisions.

Acknowledgements

This research was supported by the USDA Forest Service, Northern Research Station. The authors are grateful to Mark D. Nelson for helpful comments on an earlier version of this manuscript.

References

Abràmoff, M.D., Magalhães, P.J., Ram, S.J., 2004. Image processing with ImageJ. Biophotonics Int. 11 (7), 36–42.
Badhwar, G.D., Carnes, J.G., Austin, W.W., 1982. Use of landsat-derived temporal profiles for corn-soybean feature extraction and classification. Remote Sens. Environ. 12 (1), 57–79. https://doi.org/10.1016/0034-4257(82)90007-4.
Baig, M.H.A., Zhang, L., Shuai, T., Tong, Q., 2014. Derivation of a tasselled cap transformation based on Landsat 8 at-satellite reflectance. Remote Sens. Lett. 5 (5), 423–431. https://doi.org/10.1080/2150704X.2014.915434.
Bannari, A., Morin, D., Bonn, F., Huete, A.R., 1995. A review of vegetation indices. Remote Sens. Rev. 13 (1–2), 95–120. https://doi.org/10.1080/02757259509532298.
Bayr, C., Gallaun, H., Kleb, U., Kornberger, B., Steinegger, M., Winter, M., 2016. Satellite-based forest monitoring: spatial and temporal forecast of growing index and short-wave infrared band. Geospatial Health 11 (1). Valencia Issue. Retrieved from <http://www.geospatialhealth.net/index.php/gh/article/view/310>.
Bechtold, W.A., Patterson, P.L., 2005. The enhanced forest inventory and analysis program-national sampling design and estimation procedures.
Bradley, B.A., Jacob, R.W., Hermance, J.F., Mustard, J.F., 2007. A curve fitting procedure to derive inter-annual phenologies from time series of noisy satellite NDVI data. Remote Sens. Environ. 106 (2), 137–145. https://doi.org/10.1016/j.rse.2006.08.002.
Breiman, L., 2001. Random forests. Mach. Learn. 45 (1), 5–32. https://doi.org/10.1023/A:1010933404324.
Brooks, E.B., Thomas, V.A., Wynne, R.H., Coulston, J.W., 2012. Fitting the multitemporal curve: a Fourier series approach to the missing data problem in remote sensing analysis. IEEE Trans. Geosci. Remote Sens. 50 (9), 3340–3353.
Byrne, G.F., Crapper, P.F., Mayo, K.K., 1980. Monitoring land-cover change by principal component analysis of multitemporal Landsat data. Remote Sens. Environ. https://doi.org/10.1016/0034-4257(80)90021-8.
Chen, J., Jönsson, P., Tamura, M., Gu, Z., Matsushita, B., Eklundh, L., 2004. A simple method for reconstructing a high-quality NDVI time-series data set based on the Savitzky-Golay filter. Remote Sens. Environ. 91 (3–4), 332–344. https://doi.org/10.1016/j.rse.2004.03.014.
Chen, J., Zhu, X., Vogelmann, J.E., Gao, F., Jin, S., 2011. A simple and effective method for filling gaps in Landsat ETM+ SLC-off images. Remote Sens. Environ. 115 (4), 1053–1064. https://doi.org/10.1016/j.rse.2010.12.010.
Cohen, W.B., Fiorella, M., Gray, J., Helmer, E., Anderson, K., 1998. An efficient and accurate method for mapping forest clearcuts in the Pacific Northwest using Landsat imagery. Photogramm. Eng. Remote Sens. 64 (4), 293–299.
Crist, E.P., Cicone, R.C., 1984a. Comparisons of the dimensionality and features of simulated Landsat-4 MSS and TM data. Remote Sens. Environ. 14 (1–3), 235–246. https://doi.org/10.1016/0034-4257(84)90018-X.
Crist, E.P., Cicone, R.C., 1984b. A physically-based transformation of Thematic Mapper data – the TM Tasseled Cap. IEEE Trans. Geosci. Remote Sens. 3, 256–263.
Curran, P., 1980. Multispectral remote sensing of vegetation amount. Prog. Phys. Geogr. 4 (3), 315–341. https://doi.org/10.1177/030913338000400301.
DeFries, R., Hansen, M., Townshend, J., 1995. Global discrimination of land cover types from metrics derived from AVHRR pathfinder data. Remote Sens. Environ. 54 (3), 209–222. https://doi.org/10.1016/0034-4257(95)00142-5.
Dymond, C.C., Mladenoff, D.J., Radeloff, V.C., 2002. Phenological differences in Tasseled Cap indices improve deciduous forest classification. Remote Sens. Environ. 80 (3), 460–472. https://doi.org/10.1016/S0034-4257(01)00324-8.
Fix, E., Hodges Jr, J.L., 1951. Discriminatory analysis-nonparametric discrimination: consistency properties. DTIC Document.
Geerken, R.A., 2009. An algorithm to classify and monitor seasonal variations in vegetation phenologies and their inter-annual change. ISPRS J. Photogramm. Remote Sens. 64 (4), 422–431. https://doi.org/10.1016/j.isprsjprs.2009.03.001.
Gorelick, N., Hancher, M., Dixon, M., Ilyushchenko, S., Thau, D., Moore, R., 2017. Google Earth Engine: planetary-scale geospatial analysis for everyone. Remote Sens. Environ. https://doi.org/10.1016/j.rse.2017.06.031.
Goward, S.N., Tucker, C.J., Dye, D.G., 1985. North American vegetation patterns observed with the NOAA-7 advanced very high resolution radiometer. Vegetatio 64 (1), 3–14. https://doi.org/10.1007/BF00033449.
Hall, D.K., Riggs, G.A., Salomonson, V.V., 1995. Development of methods for mapping global snow cover using moderate resolution imaging spectroradiometer data. Remote Sens. Environ. 54 (2), 127–140. https://doi.org/10.1016/0034-4257(95)00137-P.
Hansen, M.C., Potapov, P.V., Moore, R., Hancher, M., Turubanova, S.A., Tyukavina, A., Thau, D., Stehman, S.V., Goetz, S.J., Loveland, T.R., Kommareddy, A., Egorov, A., Chini, L., Justice, C.O., Townshend, J.R.G., 2013. High-resolution global maps of 21st-century forest cover change. Science 342 (6160). 850 LP-853, Retrieved from http://science.sciencemag.org/content/342/6160/850.abstract.
Healey, S.P., Cohen, W.B., Zhiqiang, Y., Krankina, O.N., 2005. Comparison of Tasseled Cap-based Landsat data structures for use in forest disturbance detection. Remote Sens. Environ. 97 (3), 301–310. https://doi.org/10.1016/j.rse.2005.05.009.
Helmer, E.H., Brown, S., Cohen, W.B., 2000. Mapping montane tropical forest successional stage and land use with multi-date Landsat imagery. Int. J. Remote Sens. 21 (11), 2163–2183. https://doi.org/10.1080/01431160050029495.
Hermance, J.F., 2007. Stabilizing high-order, non-classical harmonic analysis of NDVI data for average annual models by damping model roughness. Int. J. Remote Sens. 28 (12), 2801–2819. https://doi.org/10.1080/01431160600967128.
Hird, J.N., McDermid, G.J., 2009. Noise reduction of NDVI time series: an empirical comparison of selected techniques. Remote Sens. Environ. 113 (1), 248–258. https://doi.org/10.1016/j.rse.2008.09.003.
Huang, C., Wylie, B., Yang, L., Homer, C., Zylstra, G., 2002. Derivation of a tasselled cap transformation based on Landsat 7 at-satellite reflectance. Int. J. Remote Sens. 23 (8), 1741–1748. https://doi.org/10.1080/01431160110106113.
Jin, S., Sader, S.A., 2005. Comparison of time series tasseled cap wetness and the normalized difference moisture index in detecting forest disturbances. Remote Sens. Environ. 94 (3), 364–372. https://doi.org/10.1016/j.rse.2004.10.012.

Jönsson, P., Eklundh, L., 2002. Seasonality extraction by function fitting to time-series of satellite sensor data. IEEE Trans. Geosci. Remote Sens. 40 (8), 1824–1832. https://doi.org/10.1109/TGRS.2002.802519.

Ju, J., Roy, D.P., 2008. The availability of cloud-free Landsat ETM+ data over the conterminous United States and globally. Remote Sens. Environ. 112 (3), 1196–1211. https://doi.org/10.1016/j.rse.2007.08.011.

Kangas, A., Maltamo, M., 2006. Forest Inventory: Methodology and Applications, vol. 10. Springer Science & Business Media.

Karlson, M., Ostwald, M., Reese, H., Sanou, J., Tankoano, B., Mattsson, E., 2015. Mapping tree canopy cover and aboveground biomass in Sudano-Sahelian woodlands using Landsat 8 and random forest. Remote Sens. 7 (8), 10017–10041.

Kauth, R.J., Thomas, G.S., 1976. The tasselled cap–a graphic description of the spectral-temporal development of agricultural crops as seen by Landsat. In LARS Symposia, p. 159.

Liaw, A., Wiener, M., 2002. Classification and regression by randomForest. R News 2 (3), 18–22.

Maxwell, S.K., Schmidt, G.L., Storey, J.C., 2007. A multi-scale segmentation approach to filling gaps in Landsat ETM+ SLC-off images. Int. J. Remote Sens. 28 (23), 5339–5356. https://doi.org/10.1080/01431160601034902.

McRoberts, R.E., 2009a. Diagnostic tools for nearest neighbors techniques when used with satellite imagery. Remote Sens. Environ. 113 (3), 489–499. https://doi.org/10.1016/j.rse.2008.06.015.

McRoberts, R.E., 2009b. A two-step nearest neighbors algorithm using satellite imagery for predicting forest structure within species composition classes. Remote Sens. Environ. 113 (3), 532–545. https://doi.org/10.1016/j.rse.2008.10.001.

McRoberts, R.E., Cohen, W.B., Næsset, E., Stehman, S.V., Tomppo, E.O., 2010a. Using remotely sensed data to construct and assess forest attribute maps and related spatial products. Scand. J. For. Res. 25 (4), 340–367. https://doi.org/10.1080/02827581.2010.497496.

McRoberts, R.E., Tomppo, E.O., Næsset, E., 2010b. Advances and emerging issues in national forest inventories. Scand. J. For. Res. 25 (4), 368–381. https://doi.org/10.1080/02827581.2010.496739.

McRoberts, R.E., 2012. Estimating forest attribute parameters for small areas using nearest neighbors techniques. For. Ecol. Manage. 272, 3–12. https://doi.org/10.1016/j.foreco.2011.06.039.

Moody, A., Johnson, D.M., 2001. Land-surface phenologies from AVHRR using the discrete Fourier transform. Remote Sens. Environ. 75 (3), 305–323.

Muja, M., Lowe, D.G., 2009. Fast approximate nearest neighbors with automatic algorithm configuration. VISAPP (1) 2 (331–340), 2.

Pickell, P.D., Hermosilla, T., Frazier, R.J., Coops, N.C., Wulder, M.A., 2016. Forest recovery trends derived from Landsat time series for North American boreal forests. Int. J. Remote Sens. 37 (1), 138–149. https://doi.org/10.1080/2150704X.2015.1126375.

Potgieter, A.B., Apan, A., Dunn, P., Hammer, G., 2007. Estimating crop area using seasonal time series of Enhanced Vegetation Index from MODIS satellite imagery. Aust. J. Agric. Res. 58 (4), 316–325. https://doi.org/10.1071/AR06279.

Pringle, M.J., Schmidt, M., Muir, J.S., 2009. Geostatistical interpolation of SLC-off Landsat ETM+ images. ISPRS J. Photogramm. Remote Sens. 64 (6), 654–664. https://doi.org/10.1016/j.isprsjprs.2009.06.001.

Reed, B.C., Brown, J.F., VanderZee, D., Loveland, T.R., Merchant, J.W., Ohlen, D.O., 1994. Measuring phenological variability from satellite imagery. J. Veg. Sci. 5 (5), 703–714. https://doi.org/10.2307/3235884.

Roerink, G.J., Menenti, M., Verhoef, W., 2000. Reconstructing cloud free NDVI composites using Fourier analysis of time series. Int. J. Remote Sens. 21 (9), 1911–1917. Retrieved from http://10.0.4.56/014311600209814.

Roy, D.P., Ju, J., Kline, K., Scaramuzza, P.L., Kovalskyy, V., Hansen, M., Loveland, T.R., Vermote, E., Zhang, C., 2010. Web-enabled Landsat Data (WELD): Landsat ETM+ composited mosaics of the conterminous United States. Remote Sens. Environ. 114 (1), 35–49. https://doi.org/10.1016/j.rse.2009.08.011.

Roy, D.P., Ju, J., Lewis, P., Schaaf, C., Gao, F., Hansen, M., Lindquist, E., 2008. Multi-temporal MODIS-Landsat data fusion for relative radiometric normalization, gap filling, and prediction of Landsat data. Remote Sens. Environ. 112 (6), 3112–3130. https://doi.org/10.1016/j.rse.2008.03.009.

Sakamoto, T., Yokozawa, M., Toritani, H., Shibayama, M., Ishitsuka, N., Ohno, H., 2005. A crop phenology detection method using time-series MODIS data. Remote Sens. Environ. 96 (3–4), 366–374. https://doi.org/10.1016/j.rse.2005.03.008.

Scharlemann, J.P.W., Benz, D., Hay, S.I., Purse, B.V., Tatem, A.J., Wint, G.R.W., Rogers, D.J., 2008. Global data for ecology and epidemiology: a novel algorithm for temporal Fourier processing MODIS data. PLoS ONE 3 (1), e1408. https://doi.org/10.1371/journal.pone.0001408.

Sellers, P.J., Tucker, C.J., Collatz, G.J., Los, S.O., Justice, C.O., Dazlich, D.A., Randall, D. A., 1994. A global 1 deg by 1 deg NDVI data set for climate studies. Part 2: the generation of global fields of terrestrial biophysical parameters from the NDVI. Int. J. Remote Sens. 15 (17), 3519–3545. https://doi.org/10.1080/01431169408954343.

Sellers, P.J., Tucker, C.J., Collatz, G.J., Los, S.O., Justice, C.O., Dazlich, D.A., Randall, D. A., 1996. A revised land surface parameterization (SiB2) for atmospheric GCMS. Part II: the generation of global fields of terrestrial biophysical parameters from satellite data. J. Clim. 9 (4), 706–737. https://doi.org/10.1175/1520-0442(1996)009<0706:ARLSPF>2.0.CO;2.

Skakun, R.S., Wulder, M.A., Franklin, S.E., 2003. Sensitivity of the thematic mapper enhanced wetness difference index to detect mountain pine beetle red-attack damage. Remote Sens. Environ. 86 (4), 433–443. https://doi.org/10.1016/S0034-4257(03)00112-3.

Stueve, K.M., Housman, I.W., Zimmerman, P.L., Nelson, M.D., Webb, J.B., Perry, C.H., Chastain, R.A., Gormanson, D.D., Huang, C., Healey, S.P., 2011. Snow-covered Landsat time series stacks improve automated disturbance mapping accuracy in forested landscapes. Remote Sens. Environ. 115 (12), 3203–3219.

Wilson, B.T., Lister, A.J., Riemann, R.I., 2012. A nearest-neighbor imputation approach to mapping tree species over large areas using forest inventory plots and moderate resolution raster data. For. Ecol. Manage. 271 (null), 182–198. https://doi.org/10.1016/j.foreco.2012.02.002.

Woodcock, C.E., Allen, R., Anderson, M., Belward, A., Bindschadler, R., Cohen, W., Gao, F., Goward, S.N., Helder, D., Helmer, E., Nemani, R., Oreopoulos, L., Schott, J., Thenkabail, P.S., Vermote, E.F., Vogelmann, J., Wulder, M.A., Wynne, R., 2008. Free access to landsat imagery. Science 320 (5879). 1011 LP-1011. Retrieved from <http://science.sciencemag.org/content/320/5879/1011.1.abstract>.

Wulder, M.A., Masek, J.G., Cohen, W.B., Loveland, T.R., Woodcock, C.E., 2012. Opening the archive: how free data has enabled the science and monitoring promise of Landsat. Remote Sens. Environ. 122, 2–10. https://doi.org/10.1016/j.rse.2012.01.010.

Yuan, F., Sawaya, K.E., Loeffelholz, B.C., Bauer, M.E., 2005. Land cover classification and change analysis of the Twin Cities (Minnesota) metropolitan area by multitemporal Landsat remote sensing. Remote Sens. Environ. 98 (2–3), 317–328. https://doi.org/10.1016/j.rse.2005.08.006.

Zhang, C., Li, W., Travis, D., 2007. Gaps-fill of SLC-off Landsat ETM+ satellite image using a geostatistical approach. Int. J. Remote Sens. 28 (22), 5103–5122. https://doi.org/10.1080/01431160701250416.

Zhang, X., Friedl, M.A., Schaaf, C.B., Strahler, A.H., Hodges, J.C.F., Gao, F., Reed, B.C., Huete, A., 2003. Monitoring vegetation phenology using MODIS. Remote Sens. Environ. 84 (3). https://doi.org/10.1016/S0034-4257(02)00135-9.

Zheng, S., Cao, C., Dang, Y., Xiang, H., Zhao, J., Zhang, Y., Wang, X., Guo, H., 2014. Retrieval of forest growing stock volume by two different methods using Landsat TM images. Int. J. Remote Sens. 35 (1), 29–43. https://doi.org/10.1080/01431161.2013.860567.

Zhu, X., Liu, D., 2015. Improving forest aboveground biomass estimation using seasonal Landsat NDVI time-series. ISPRS J. Photogramm. Remote Sens. 102 (Suppl. C), 222–231. https://doi.org/10.1016/j.isprsjprs.2014.08.014.

Zhu, Z., Woodcock, C.E., Olofsson, P., 2012. Continuous monitoring of forest disturbance using all available Landsat imagery. Remote Sens. Environ. 122, 75–91. https://doi.org/10.1016/j.rse.2011.10.030.